Paleoceanography and Paleoclimatology

AGU ADVANCING EARTH AND SPACE SCIENCE

RESEARCH ARTICLE
10.1029/2022PA004573

Nitrogen Isotope Record From a Mid-oceanic Paleo-Atoll Limestone to Constrain the Redox State of the Panthalassa Ocean in the Capitanian (Late Guadalupian, Permian)

Masafumi Saitoh[1,2,3,4], Manabu Nishizawa[1,5], Kazumi Ozaki[2,6], Masayuki Ikeda[7], Yuichiro Ueno[2,5,6], Ken Takai[5], and Yukio Isozaki[8]

[1]Laboratory of Ocean-Earth Life Evolution Research (OELE), Japan Agency for Marine-Earth Science and Technology (JAMSTEC), Yokosuka, Japan, [2]Earth-Life Science Institute, Tokyo Institute of Technology, Tokyo, Japan, [3]School of Geosciences and Civil Engineering, Kanazawa University, Kanazawa, Japan, [4]The University Museum, The University of Tokyo, Tokyo, Japan, [5]Institute for Extra-cutting-edge Science and Technology Avant-garde Research (X-star), Super-cutting-edge Grand and Advanced Research (SUGAR) Program, Japan Agency for Marine-Earth Science and Technology (JAMSTEC), Yokosuka, Japan, [6]Department of Earth and Planetary Sciences, Tokyo Institute of Technology, Tokyo, Japan, [7]Department of Earth and Planetary Environmental Science, The University of Tokyo, Tokyo, Japan, [8]Department of Earth Science and Astronomy, The University of Tokyo, Tokyo, Japan

Abstract The Capitanian stage is characterized by marine anoxia possibly related to the extinction, although the global redox structure of the Capitanian ocean has not been constrained. We newly report a nitrogen isotope ($\delta^{15}N$) record from a paleo-atoll limestone at the top of a mid-Panthalassan seamount to constrain the spatial extent and duration of the Capitanian marine anoxia. The $\delta^{15}N$ value of limestone after acid treatment is substantially high for ~5-Myr up to +28‰, the highest through the Phanerozoic oceans, suggesting that the nitrogen source (nitrate) was substantially enriched in ^{15}N via denitrification within subsurface oxygen-deficient zones (ODZs; $O_2 < 5$ μM). Numerical modeling of nitrogen isotope dynamics in the upwelling system along the seamount suggests that the possible minimum $\delta^{15}N$ value of a global deep-oceanic nitrate reservoir was ca. +9‰ in the Capitanian (~4‰ higher than at the present). Furthermore, a redox-dependent nitrogen isotope mass balance model constrained the global redox structure of the Capitanian superocean. Substantially reducing conditions ($O_2 \leq 20$ μM) prevailed at intermediate water depths (100–1,000 m), in association with expanded ODZs with anoxic/euxinic cores along continental margins (≥ ~0.4% of global ocean volume), while the deep-ocean remained to be more oxidizing ($O_2 \leq 60$ μM). The enhanced open-ocean productivity associated with the low sea-level and high nutrient flux to the ocean resulted in the global ocean deoxygenation during the cooling stage. Our model is consistent with previous geologic observations and with a possible link between the long-term (~5-Myr) development of marine dysoxia and the extinction.

Plain Language Summary The Capitanian stage is a peculiar stage characterized by several environmental changes including marine anoxia, possibly related to the large extinction. Previous studies reported the evidence for marine anoxia developed at least locally in the Capitanian, although the spatial extent and duration of anoxia in the superocean Panthalassa in the stage have been poorly constrained. Bioavailable nitrogen is essential for life and the nitrogen isotopic composition of sedimentary record is useful to reconstruct the global nitrogen cycle in association with oceanic redox condition in the past. We report a ~5-Myr-long nitrogen isotope record from a shallow-water limestone in the lost mid-superocean during the Capitanian. This unique record reveals major changes in global nitrogen cycle in the stage, that is, the appearance of a substantially ^{15}N-enriched oceanic nitrate reservoir indicating enhanced anaerobic respiration under reducing conditions. Numerical modeling further constrains that the reducing water masses ($O_2 < 20$ μM) prevailed at intermediate water depths (100–1,000 m) in the superocean, in association with the expanded oxygen-deficient zones with anoxic/euxinic cores developed along the continental margins (at least twice as much as in the modern oceans). Our new model is consistent with the scenario that the long-term subsurface anoxia/euxinia contributed to the shelf extinction.

Key Points:

- N isotope record from the mid-Panthalassa suggesting expanded oxygen-deficient zones in mid-water depths (>~0.4% of global ocean volume)
- Substantially reducing ocean in association with the low sea-level, high nutrient flux to the ocean, and enhanced open-ocean productivity
- A possible link between the long-term (~5-Myr) deep-water anoxia/euxinia along the continental margins and the shelf extinction

Masafumi Saitoh and Manabu Nishizawa contributed equally to this work.

Supporting Information:

Supporting Information may be found in the online version of this article.

Correspondence to:

M. Saitoh and M. Nishizawa,
msaitoh@um.u-tokyo.ac.jp;
m_nishizawa@jamstec.go.jp

Citation:

Saitoh, M., Nishizawa, M., Ozaki, K., Ikeda, M., Ueno, Y., Takai, K., & Isozaki, Y. (2023). Nitrogen isotope record from a mid-oceanic paleo-atoll limestone to constrain the redox state of the Panthalassa ocean in the Capitanian (Late Guadalupian, Permian). *Paleoceanography and Paleoclimatology*, *38*, e2022PA004573. https://doi.org/10.1029/2022PA004573

Received 25 OCT 2022
Accepted 11 MAY 2023

Author Contributions:

Conceptualization: Masafumi Saitoh
Funding acquisition: Masafumi Saitoh, Manabu Nishizawa, Yukio Isozaki

1. Introduction

Bioavailable nitrogen (so-called "fixed-N") is essential for organisms and is a major component in the oceanic biogeochemical cycle in Earth history (e.g., Falkowski, 1997). Fixed-N exists most abundantly as nitrate (NO_3^-)

Investigation: Masafumi Saitoh, Manabu Nishizawa, Kazumi Ozaki, Masayuki Ikeda, Yuichiro Ueno, Ken Takai, Yukio Isozaki
Methodology: Masafumi Saitoh, Manabu Nishizawa, Kazumi Ozaki, Masayuki Ikeda, Yuichiro Ueno, Ken Takai, Yukio Isozaki
Resources: Yukio Isozaki
Validation: Masafumi Saitoh
Writing – original draft: Masafumi Saitoh, Manabu Nishizawa
Writing – review & editing: Kazumi Ozaki, Masayuki Ikeda, Yuichiro Ueno, Ken Takai, Yukio Isozaki

in the modern oxic oceans, and microbial nitrogen fixation and denitrification are a major source and sink, respectively, of the oceanic fixed-N pool. Fixed-N is generally supplied to the surface ocean via nitrogen fixation, the biological reduction of dinitrogen (N_2) to ammonium (NH_4^+), by diazotrophic cyanobacteria. In contrast, denitrification, an anaerobic process of nitrate reduction to N_2 via oxidation of organic matter, occurs in the oxygen-deficient zones (ODZs; the O_2 concentration <5 μM) at intermediate water depths (100–1,000 m) and in marine sediments (Note 1 in Appendix A) (Codispoti et al., 2005; Dalsgaard et al., 2014). Nitrogen isotope fractionation via water-mass denitrification is large up to 25‰, whereas the fractionation via benthic denitrification in sediments is small (<3‰) (e.g., Brandes & Devol, 2002). In a simplified model of the global fixed-N cycle, the nitrogen isotopic composition ($\delta^{15}N$) of an oceanic nitrate reservoir ($\delta^{15}N_{NO3}$) is determined by a balance between water-mass and benthic denitrification on a global scale and thus by the global oceanic redox conditions.

The $\delta^{15}N$ value of organic matter in marine sedimentary record has been suggested to be useful for reconstructing the $\delta^{15}N_{NO3}$ value and the global fixed-N cycle in association with oceanic redox conditions in the past (e.g., Robinson et al., 2012). Based on a comprehensive $\delta^{15}N$ compilation through the Phanerozoic, Algeo et al. (2014) suggested ∼100-Myr-scale $\delta^{15}N$ fluctuations in coincidence with the long-term variation in climate and eustacy. In their model, greenhouse climate modes were characterized by low $\delta^{15}N$ values of sediments (−2‰ to +2‰) with the reduced OMZs whereas icehouse climate modes were characterized by high $\delta^{15}N$ values (up to +8‰) with the expanded OMZs. The OMZ expansions during icehouse climate modes were caused by an increased nutrient influx from the continents to the oceans and enhanced surface-ocean productivity. Kast et al. (2019) reported the $\delta^{15}N$ value of foraminifera shell-bound organic matter during the Paleocene–Eocene transition and found a 10-Myr-long $\delta^{15}N$ decline from ca. +15‰ to +3‰ coincident with global cooling and oceanic oxidation associated with the Asia–India collision. These studies illustrated that the global fixed-N cycle has been controlled largely by oscillation in oceanic redox condition on the geological time scales.

The ca. 264.3–259.6 Ma Capitanian, the Late Guadalupian stage (Henderson et al., 2020), is characterized by the large extinction in marine and terrestrial realms which occurred ca.7.6 Myr before the larger biotic catastrophe at the end-Permian (Bond, Hilton, et al., 2010; Jin et al., 1994; Stanley & Yang, 1994). Several geologic phenomena in the Capitanian have been proposed as the cause of the extinction, such as the eruption of the Emeishan flood basalts in South China (e.g., Wignall et al., 2009; Zhou et al., 2002), a eustatic sea-level fall (Jin et al., 1994), climate warming and oceanic acidification (Clapham & Payne, 2011), cooling (Isozaki et al., 2007a; and b), and marine anoxia/euxinia (Saitoh et al., 2013a, 2013b; Yan et al., 2013). In particular, the emergence of anoxic/sulfidic conditions along the continental margins in the Capitanian oceans has been reported in South China (Kametaka et al., 2005; Saitoh et al., 2013a, 2014a; Shi et al., 2016; Wei et al., 2016, 2019; G.J. Zhang et al., 2015; B. Zhang et al., 2018, 2019a, 2021), NW Pangea (Bond et al., 2020; G.J. Zhang et al., 2015), and the Boreal Realm (Bond et al., 2015) (Figure 1a). Although the depositional setting, depth, and age of the sediments at each section were different from each other in these regions, the growing body of evidence suggests that the anoxic/sulfidic water masses prevailed widely along the continental margins, persisting as a potential stress for shallow-marine biota (Saitoh et al., 2014; Wei et al., 2019). In addition, the $\delta^{15}N$ value of organic matter in some of those anoxic/euxinic sediments is substantially high (+8‰ to +14‰) and suggests denitrification in the reducing deep-water masses along the continental margins, possibly in association with the intensified ODZs (Saitoh et al., 2014; Schoepfer et al., 2012). Apart from the anoxia/euxinia along the continental margins, Isozaki (1997) proposed that the deep part of the Panthalassic ocean was under prolonged oxygen-depleted conditions from the Capitanian to the Early Triassic (superanoxia). However, the onset timing of superanoxia is still controversial partly due to poor age constraints on mid-Panthalassan pelagic sediments with no index conodont (Fujisaki et al., 2019; Isozaki, 2009; Kakuwa, 2008; Kato et al., 2002; Matsuo et al., 2003; Onoue et al., 2021). The contribution of Capitanian marine anoxia/euxinia to the shallow-marine extinction is still largely uncertain because the global oceanic redox structure in the stage has been poorly constrained so far.

In order to constrain the redox structure of the Capitanian oceans from a global perspective, we focus on a paleo-atoll limestone accumulated originally at the top of an ancient seamount in mid-Panthalassa during the stage (Figure 1). Pre-Jurassic mid-oceanic paleo-atoll carbonates, as well as deep-sea cherts, have been generally regarded as a rare sedimentary archive of environmental changes in the pelagic realms of lost oceans (Isozaki, 2014). In the present study, we report a high-resolution $\delta^{15}N$ profile of a mid-Panthalassan paleo-atoll limestone, now located in central Japan as an allochthonous block in an accretionary complex (Figure 1b). The analyzed limestone records substantially high $\delta^{15}N$ values with large $\delta^{15}N$ oscillation. In particular, its large amplitude and estimated long periodicity are distinct from those of previously-known $\delta^{15}N$ oscillation in the

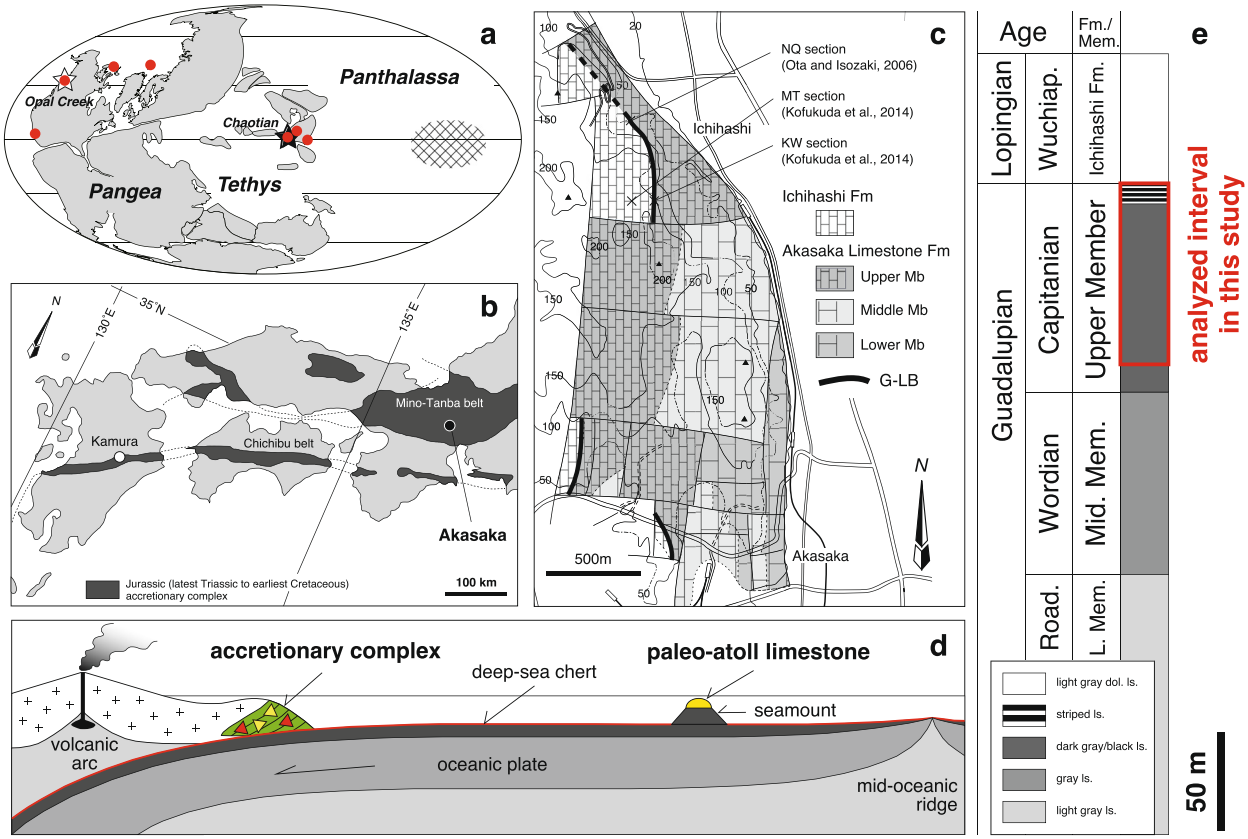

Figure 1. Index maps and stratigraphy of the paleo-atoll limestone at Akasaka in central Japan. (a) Guadalupian paleogeography (modified from Muttoni et al., 2009) with the estimated location of the mid-Panthalassan seamount on which the Akasaka limestone accumulated (hatched area). Black and white stars represent the Chaotian and Opal Creek sections, respectively. A red dot shows a section, at which evidence for anoxia has been reported (Bond et al., 2015, 2020; Saitoh et al., 2013a; Shi et al., 2016; Yan et al., 2013; Zhang et al., 2015). (b) The Akasaka section in the Mino–Tanba belt, central Japan. A white dot represents the Kamura section (Isozaki et al., 2007a; Ota & Isozaki, 2006). (c) Geologic map of the Akasaka limestone. (d) Schematic diagram of the ridge-subduction system with mid-oceanic sediments. A fragment of the mid-oceanic sediments (yellow and red triangles) is preserved as an allochthonous block in the accretionary complex. (e) Stratigraphy of the Akasaka limestone. Road.: Roadian, Wuchiap.: Wuchiapingian, L. Mem.: Lower Member, Mid. Mem.: Middle Member, Fm.: Formation, ls.: limestone, dol.: dolomitic.

Phanerozoic. To constrain biogeochemical and oceanographic conditions quantitatively for these characteristic features of $\delta^{15}N$ record from mid-Panthalassa, we employ and connect two numerical models: one of the global oceanic fixed-N cycle and the other of the local upwelling system along the seamount, at the top of which the analyzed limestone accumulated. Based on a constraint from the first global model, we reconstruct the oceanic fixed-N cycle and estimate the global volume of the ODZs in the Capitanian ocean. Furthermore, based on the second model, we reconstruct oscillation in the local upwelling system along the seamount, which could have caused the observed $\delta^{15}N$ fluctuations, and speculate its possible driving force.

2. Geological Setting and Stratigraphy

The pre-200 Ma mid-oceanic sedimentary rocks have been generally lost due to subduction driven by plate tectonics (Figure 1), except for an allochthonous block incorporated into an accretionasry complex (e.g., Isozaki, 2009; Isozaki et al., 1990). Particularly, the Mesozoic accretionary complexes in Japan contain allochthonous blocks of the Permian deep-sea cherts and paleo-atoll carbonates, which originally accumulated several thousand kilometers away from the eastern margin of South China in low-latitude mid-Panthalassa (Figure 1) (e.g., Isozaki, 1997; Isozaki et al., 2007a; Kanmera & Nishi, 1983; Matsuda & Isozaki, 1991). The Permian limestone at Akasaka in Gifu Prefecture, central Japan (e.g., Ota & Isozaki, 2006), is such a paleo-atoll limestone originally accumulated at the top of a mid-oceanic seamount in the western Panthalassa during the Guadalupian–Lopingian transition. It is now exposed as a kilometer-sized block within the Jurassic mudstone matrix of the accretionary complex in the

Mino-Tanba belt; within the block, the Permian limestone strikes in N–S and dips at 40° to the west in the Middle Jurassic accretionary complex of the Mino–Tanba belt (Kofukuda et al., 2014; Ota & Isozaki, 2006; Sano, 1988). Detailed litho-, bio-, and chemo-stratigraphies of the Akasaka limestone have been examined by previous studies (e.g., Akasaka Research Group, 1956; Isozaki & Ota, 2001; Kani et al., 2013; Kofukuda et al., 2014; Ota & Isozaki, 2006; Ozawa & Nishiwaki, 1992; Sakagami, 1980; Zaw Win, 1999, 2000).

The Permian limestone at Akasaka (>250-m-thick in total) is composed of the Guadalupian Akasaka Limestone Formation and the overlying Lopingian Ichihashi Formation (Figure 1) (Akasaka Research Group, 1956; Kofukuda et al., 2014; Ota & Isozaki, 2006; Ozawa & Nishiwaki, 1992; Zaw Win, 1999). A non-carbonate bed in greenish color (<1-cm-thick) is intercalated between the Akasaka Limestone and Ichihashi formations, which marks an erosion horizon with a hiatus (Kofukuda et al., 2014). The Akasaka Limestone Formation is composed of fresh and pure gray/black bioclastic limestone with various shallow-marine fossils including fusulines, algae, and large bivalves. This formation consists of three stratigraphic units: the Lower, Middle, and Upper members, in ascending order. The Lower and Middle members (>170-m-thick in total) is composed of gray and dark gray bioclastic limestones, respectively, with large fusulines. The Upper Member of the Akasaka Limestone Formation, over 120-m-thick, is mainly composed of thickly bedded dark gray to black bioclastic limestone with abundant calcareous algae and large fusulines. In this study, we analyzed this Upper Member limestone. The uppermost part of the Upper Member (ca. 9-m-thick) is composed of light/dark gray striped limestone. The overlying Ichihashi Formation, over 96-m-thick, is composed of gray to white dolomitic limestone with abundant small fusulines. Based on lithofacies characteristics, Zaw Win (2000) and Kofukuda et al. (2014) interpreted that the Akasaka Limestone and Ichihashi formations were deposited in subtidal and intertidal settings, respectively, at the top of the seamount.

Fusuline is a main dating clue because no index conodont/ammonoid was reported to date from the shallow-water Akasaka limestone. Based on the fusuline biostratigraphy, the stratigraphic units of the Akasaka limestone are correlated as follows (Kobayashi, 2011; Kofukuda et al., 2014; Ota & Isozaki, 2006; Zaw Win, 1999, 2000): the Lower Member of the Akasaka Limestone Formation to the Roadian (Early Guadalupian), the Middle Member of the formation to the Roadian to Wordian (Middle Guadalupian), the Upper Member of the formation to the Capitanian, and the Ichihashi Formation to the Wuchiapingian (Early Lopingian), respectively (Figure 1e). Two-stepped extinction is recorded in the uppermost 20-m-thick part of the Upper Member (Kofukuda et al., 2014). The Guadalupian–Lopingian boundary (G–LB) is assigned to the base of the Ichihashi Formation. This study analyzed the Upper Member limestone, which is correlated particularly to the early to latest Capitanian.

3. Materials and Analytical Methods

3.1. Nitrogen Isotopic Analyses

Fresh rock samples of the Upper Member of the Akasaka Limestone Formation were collected from the outcrop and by scientific drilling. For the isotope measurements, we followed a conventional "rinse method" in previous studies for Precambrian/Paleozoic sedimentary records (e.g., Fujisaki et al., 2019; Saitoh et al., 2014). After cutting by a disk saw, a thin (~5 mm thick) rock slab was fragmented roughly into small pieces (~1 cm in diameter) in an agate mill. The rock pieces were then cleaned ultrasonically by distilled water (10 min, two times) and pure ethanol (10 min, two times) to remove any dust and organics on their surface. The pieces were dried up at room temperature and ~10 g of sample was powdered by using an agate mill. The sample powder was reacted with 10 M HCl (made of Super Special Grade HCl, 35.0%–37.0%, FUJIFILM Wako Pure Chem. Corp., ID: 083–03435) at room temperature overnight to dissolve carbonate. The acid residue was purified by repeated centrifugation with distilled water and was dried at 70°C overnight. <20 mg of the dried residue was placed in a tin cup, and the nitrogen isotopic value was measured by using a ThermoFinnigan DELTAplus Advantage mass spectrometer coupled with an EA 1112 Series FLASH Elemental Analyzer at JAMSTEC. The nitrogen isotopic composition is reported in ‰ relative to atmospheric N_2 according to $\delta^{15}N = (R_{sample}/R_{standard} - 1) \times 1{,}000$, where R is the isotopic ratio ($^{15}N/^{14}N$) of the sample and the standard. The analytical reproducibility of the $\delta^{15}N$ value determined by replicate analyses of the laboratory standards is 0.4‰ (1σ) (Table S1 in Supporting Information S1).

We use the notation $\delta^{15}N_{acid.}$ for the $\delta^{15}N$ value of the Akasaka limestone below to specify the acid treatment before isotope measurement. The influence of nitrogen contamination during the pre-measurement procedure

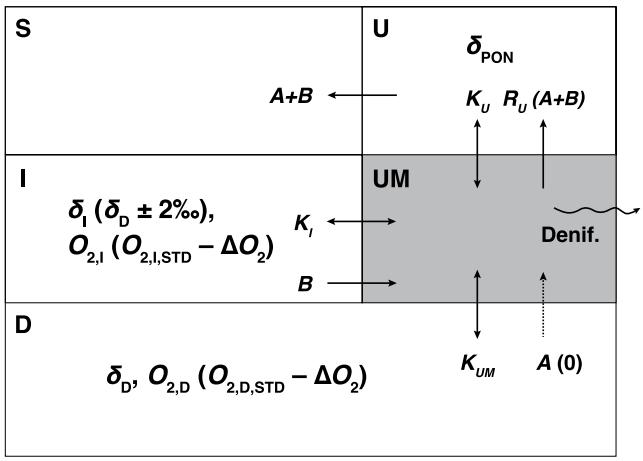

Figure 2. Fix-boxes model of the local upwelling system along the Akasaka seamount, modified after Canfield (2006) and Boyle et al. (2013). We interpret that the $\delta^{15}N$ value of the analyzed Akasaka limestone records δ_{PON}, the $\delta^{15}N$ value of fixed-N in the surface box U (the local surface ocean around the top of the seamount). Denif.: denitrification. δ_I and δ_D: the $\delta^{15}N$ value of nitrate in the boxes I and D. $O_{2,I}$ and $O_{2,D}$: the O_2 concentration of the boxes I and D, respectively. ΔO_2 is introduced as a parameter of the global oceanic redox conditions. See the main text for details.

and from clay minerals on the $\delta^{15}N_{acid.}$ value of the analyzed samples was negligible (Text S1 and S2, Tables S3 and S4 in Supporting Information S1). The total nitrogen (TN) and total organic carbon (TOC) contents of the initial sediments (before the acid treatment) were quantified based on the weight data and the intensity measured by TCD (Tables S1 and S2 in Supporting Information S1). See Supporting Information for more details of the isotope analyses and TN and TOC quantification.

3.2. Spectral Analysis

To assess the cyclicity of stratigraphic variations inthe Capitanian Akasaka $\delta^{15}N_{acid.}$ fluctuations, we performed wavelet analyses on depth series of $\delta^{15}N_{acid.}$ records using a series of Matlab algorithms modified from those developed by Torrence and Compo (1998). This program can identify whether peaks in the spectrum of the time series are significant against the red-noise (autoregressive lag1) background spectrum.

3.3. Modeling

We employed two models to examine biogeochemical and oceanographic processes in the Capitanian superocean, which were recorded in the Akasaka limestone.

3.3.1. Local Upwelling Model

We focused on the depositional setting of the Akasaka limestone for the first model. It is a paleo-atoll limestone accumulated at the top of a mid-oceanic seamount in low latitudes (Figure 1d) (Kofukuda et al., 2014), where a deep water-mass likely upwelled along the seamount, as on the Galapagos islands in the modern equatorial eastern Pacific (e.g., Forryan et al., 2021). As discussed later in Section 5.1, the $\delta^{15}N_{acid.}$ value of the Akasaka limestone is interpreted to record the value of fixed-N assimilated into biomass in the surface ocean around the seamount. We employed a five-boxes model modified after Canfield. (2006) and Boyle et al. (2013), to examine the $\delta^{15}N$ value of particulate organic nitrogen (PON) in the surface ocean box U around the seamount top (δ_{PON}) (Figure 2).

We focus particularly on the intermediate water depth of the upwelling region (the box UM). We calculated the export production (*EP*) and the concentrations of molecular oxygen (O_2), nitrate (*N*), ammonium (N^R), phosphate, and hydrogen sulfide (H_2S) in the box UM based on the steady-state mass balance equations and boundary conditions (e.g., the concentration of chemical species in the outer open-ocean (the boxes I and *D*); Table A1). The steady-state mass balance equations include the terms of water mass transport process between UM and surrounding boxes with following parameters: the vertical water exchange rate between U and UM (K_U), the vertical water exchange rate between UM and the deep-ocean box D (K_{UM}), the horizontal water exchange rate between UM and the open-ocean intermediate layer box I (K_I), the advective upwelling from D to UM (*A*), and the advective flow from I to UM (*B*) (Figure 2). The upwelling rate of water mass from UM to U (R_U) is determined by the sum of *A* and *B* ($R_U = A + B$), and varied from 0 cm/hr to 2.0 cm/hr, which is a typical range of R_U observed in the modern ODZs (Canfield, 2006). The reference values used for the other parameters are listed in Table A1. When the O_2 concentration of the box UM ($O_{2,UM}$) decreases to zero by in-situ aerobic respiration of exported organic matter, water-mass denitrification occurs and increases the $\delta^{15}N$ value of residual nitrate in the box, which eventually increases δ_{PON} as seen in the next paragraph.

We assumed that, in the surface water region in the upwelling system around the seamount (box U), upwelled nitrate and ammonium from the box UM was assimilated completely into biomass (N_U and N^R_U are zero) with no isotope fractionation. When nitrogen fixation is limited in box U ("non-N-fixation case" in the original model; Boyle et al., 2013), δ_{PON} is simply determined by the nitrogen isotope mass balance in the box UM:

$$\delta_{PON} = \frac{\delta_{UM} N_{UM} + \delta^R_{UM} N^R_{UM}}{N_{UM} + N^R_{UM}}, \quad (1)$$

where δ_{UM} and δ^{R}_{UM} are the $\delta^{15}N$ value of nitrate and ammonium in the box UM, respectively. The variables on the right-hand side are obtained based on steady-state mass balance equations. (When nitrogen fixation is not inhibited in box U, δ_{PON} is not expressed by Equation A1 but by Equation A18 in Appendix B.)

Equation 1 means that δ_{PON} is a function of δ_{UM} in the present upwelling model, and δ_{UM} is largely influenced by the nitrogen isotopic composition of nitrate in the deep-ocean box D (δ_D). This is because nitrate in the box UM is supplied not only from box I via the water exchange (K_{UM}) and advective flow (B) but also from box D via water exchange (K_{UM}). (Note that the advective upwelling flow from D to UM (A) is assumed to be constantly zero (Table A1).) Furthermore, in the modern oceans, the difference between the nitrogen isotopic composition of nitrate in box I (δ_I) and δ_D is at most ~2‰ (Text S5 in Supporting Information S1). Accordingly, δ_{PON} in the surface box U is regarded to be an indirect recorder of δ_D in the present model.

In general, the nitrogen isotopic composition of a deep-oceanic nitrate reservoir (δ_D) reflects the oceanic redox conditions on a global scale (as mentioned later in Section 3.3.2). On the other hand, as mentioned above, δ_{PON} in the surface box U is an indirect recorder of δ_D in the present upwelling model. We examined the specific influence of global oceanic redox conditions on δ_{PON} in the model, and focused particularly on the O_2 concentration of the outer open-ocean: the boxes I and D (Figure 2). (Note that the sum of the volume of the boxes I and D can be assumed to be >95% of global ocean volume, and thus the O_2 concentrations of these two boxes can be regarded practically as a proxy for the global oceanic redox conditions.) We defined the O_2 concentrations of the boxes I and D as $O_{2,I}$ and $O_{2,D}$, respectively, and particularly determined the $O_{2,I}$ and $O_{2,D}$ values at the "standard oceanic condition" ($O_{2,I,STD}$ and $O_{2,D,STD}$) are 100 and 140 μM, respectively, according to the typical O_2 concentration of the modern oceans (e.g., Lam & Kuypers, 2011). In the reducing ocean, the $O_{2,I}$ and $O_{2,D}$ values should be lower than 100 and 140 μM, respectively, and we introduced ΔO_2 as a parameter of the global oceanic redox conditions:

$$\Delta O_2 = O_{2,I} - O_{2,I,STD} = O_{2,D} - O_{2,D,STD} \quad (2)$$

We defined $O_{2,I}$ to be 0 μM when ΔO_2 is lower than −100 μM. Also, when ΔO_2 is −140 μM ($O_{2,I} = O_{2,D} = 0$ μM), we regarded that the ocean was "nitrogenous" (Note 2 in Appendix A).

δ_I and δ_D are the $\delta^{15}N$ value of seawater nitrate in the open-ocean boxes I and D, respectively (Figure 2; Table A1). Based on the modern observations (e.g., Fripiat et al., 2021), we assumed that δ_I ranges from δ_D – two‰ to $\delta_D + 2$‰ (Text S5 in Supporting Information S1). We examined the conditions of ΔO_2 and δ_D (δ_I) under which the fluctuation range of δ_{PON} can fully cover the Akasaka $\delta^{15}N$ range, within the supposed range of R_U (0–2.0 cm/hr).

3.3.2. Global Nitrogen Isotope Mass Balance

The second model deals with the nitrogen isotopic composition of a global deep-oceanic nitrate reservoir ($\delta^{15}N_{NO3}$) with the assumed steady state in the oceanic nitrogen budget (Figure 3a) (Algeo et al., 2014). The $\delta^{15}N_{NO3}$ value is expressed in the following simple nitrogen isotope mass balance equation in the model:

$$\delta_{NO_3^-} = -\varepsilon_{WD} f - \varepsilon_{SD}(1 - f) + \left(\delta_{N_2} + \varepsilon_{fix}\right), \quad (3)$$

where δ denotes the $\delta^{15}N$ value, ε_{WD} and ε_{SD} are nitrogen isotope fractionation during water-mass and benthic denitrification, respectively, ε_{fix} is isotope fractionation via nitrogen fixation, $\delta^{15}N_{N2}$ is the nitrogen isotopic composition of atmospheric N_2, and f is the global proportion of water-column denitrification to benthic denitrification (Figure 3a). (In the model, the term "denitrification" includes not only heterotrophic denitrification (sequential reduction of nitrate to N_2) but also anammox coupled with nitrate reduction to nitrite.) The parameter values used in the model with their potential ranges are summarized in Table 1.

This model predicts that the $\delta^{15}N_{NO3}$ value records the global oceanic redox conditions since the f value depends essentially on the volume of ODZs on a global scale. For example, the averaged $\delta^{15}N_{NO3}$ value in the modern oceans is ca. +4.9‰ (Robinson et al., 2012), and the f value is calculated to be 0.27 at $\varepsilon_{WD} = -20$‰, $\varepsilon_{SD} = -2$‰, and $\varepsilon_{fix} = -2$‰ (white circle in Figure 3b). This value is consistent with the independent estimation that ca. 30% of fixed-N loss from the modern oceans is responsible for denitrification in the ODZs that comprise only 0.2% of the global ocean water-mass (Bianchi et al., 2012; Galloway, 2014). In contrast, the $\delta^{15}N_{NO3}$ value is predicted to be 18 ± 3‰ in the "nitrogenous" ocean in which the ODZs expand entirely to the boxes I and D while fixed-N in these boxes is predominantly nitrate. In the "nitrogenous" ocean, the O_2 concentration of these boxes is less than 5 μM (Appendix A) and denitrification occurs everywhere in the boxes. The f value is expected to be one in that case (black dot in Figure 3b).

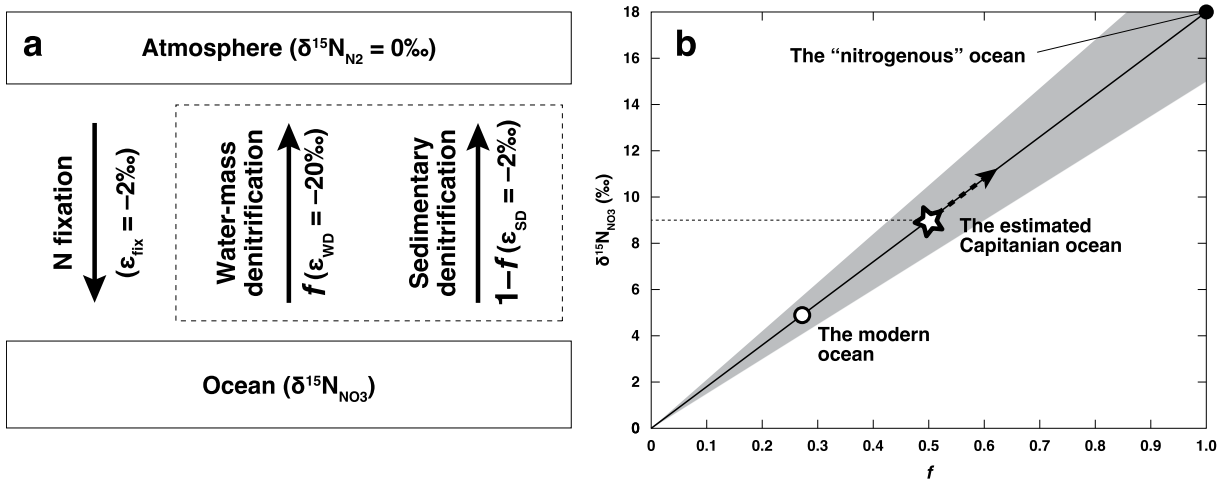

Figure 3. Model scheme for the Akasaka $\delta^{15}N_{acid.}$ record. (a) Simplified global nitrogen isotope mass balance after Algeo et al. (2014). ε_{WD} and ε_{SD} are nitrogen isotope fractionation during water-mass and benthic denitrification, respectively, and ε_{fix} is isotope fractionation via nitrogen fixation. $\delta^{15}N_{N2}$ is the isotope ratio of atmospheric N_2. With the fixed fractionation factors (ε_{WD}, ε_{SD}, and ε_{fix}) and $\delta^{15}N_{N2}$, the $\delta^{15}N$ value of an oceanic nitrate reservoir ($\delta^{15}N_{NO3}$) is determined by f, the global proportion of water-column denitrification to benthic denitrification. (b) Relationship between f and $\delta^{15}N_{NO3}$ on the global nitrogen isotope mass balance (a). White and black dots represent the modern and "nitrogenous" oceans, respectively. A star represents the most potentially oxidizing condition in the Capitanian ocean, constrained in this study. See the main text for more details. Nitrogen isotopic fractionation via denitrification is assumed to be 20 ± 3‰ (gray area), and the $\delta^{15}N_{NO3}$ value in the modern oceans is assumed to be +4.9‰ (Robinson et al., 2012).

The $\delta^{15}N_{NO3}$ value in the global isotope mass balance corresponds to δ_D in the local upwelling model (Figure 2), as the volume of the deep-ocean box D can be assumed to be >95% of global ocean volume. This is the junction between the local upwelling model (Figure 2) and the global isotope mass balance (Figure 3) in the present modeling.

4. Results

4.1. Akasaka $\delta^{15}N_{acid.}$ Record

Table 2 lists all of the measurements of the $\delta^{15}N_{acid.}$ value, the TN and TOC contents, and the TOC/TN atomic ratio of the analyzed Akasaka limestone. Geochemical cross plots of the data are shown in Figure 4. The stratigraphic $\delta^{15}N_{acid.}$ record of the Akasaka limestone is characterized by (a) substantially high values through the succession, and (b) large and periodic fluctuations (Figure 5). The $\delta^{15}N_{acid.}$ values are consistently high at Akasaka (+19.4‰ on average). In particular, the maximum value of +28.3‰ is the highest in the previously-reported stratigraphic marine $\delta^{15}N$ records in the Phanerozoic (e.g., Algeo et al., 2014; Kidder & Worsley, 2010), and the second highest in all the sub-greenschist sediments in Earth history (Stüeken et al., 2015; Thomazo et al., 2011).

Table 1
Parameters for the Global Nitrogen Isotope Mass Balance of an Oceanic Nitrate Reservoir

Parameters	Label	Range (default parameter value)	Unit	Ref.
Nitrogen isotopic composition of a global oceanic nitrate reservoir	$\delta^{15}N_{NO3}$		‰	
Proportion of water-mass denitrification to benthic denitrification	F		-	
Nitrogen isotope fractionation via Nitrogen fixation[a]	ε_{fix}	0 to −7 (−2)	‰	Nishizawa et al. (2014), Zhang et al. (2014)
Nitrogen isotopic composition of atmospheric N_2[b]	$\delta^{15}N_{N2}$	0 (0)	‰	Sano & Pillinger (1990), Nishizawa et al. (2007)
Nitrogen isotope fractionation via water-mass denitrification[c]	ε_{WD}	−20 ± 3 (−20)	‰	Brandes & Devol (2002), Sigman & Fripiat (2019)
Nitrogen isotope fractionation via sedimentary denitrification[d]	ε_{SD}	−1.5 ± 1.5 (−2)	‰	Brandes & Devol (2002)

[a]Depending on nitrogenase types. [b]Rather consistent through Earth history. [c]The term "denitrification" includes not only heterotrophic denitrification (sequential reduction of nitrate to N_2) but also anammox coupled with nitrite reduction to N_2 in the model. [d]Little isotope fractionation due to a reservoir effect.

Table 2
Akasaka $\delta^{15}N_{acid}$

Sample ID	Formation	Member	Thickness (m)	$\delta^{15}N_{acid.}$ (‰)	TN (ppm)	TOC (ppm)	C/N atomic
A31	Akasaka Limestone	Upper Member	117.9		1	16	28
A33.5	Akasaka Limestone	Upper Member	115.9		1	83	90
A34.4	Akasaka Limestone	Upper Member	115.2	15.6	2	71	46
A35.6	Akasaka Limestone	Upper Member	114.2	13.3	13	484	43
A36.8	Akasaka Limestone	Upper Member	113.3	11.9	4	100	26
A36.9	Akasaka Limestone	Upper Member	113.2	14.0	5	101	24
A37.5	Akasaka Limestone	Upper Member	112.7	12.5	6	125	25
A38.5	Akasaka Limestone	Upper Member	111.9	11.3	6	87	17
A38.8	Akasaka Limestone	Upper Member	111.7	16.7	16	291	21
A39.8	Akasaka Limestone	Upper Member	110.9	15.7	5	84	18
A40.6	Akasaka Limestone	Upper Member	110.2	20.4	7	451	74
A41	Akasaka Limestone	Upper Member	109.9	21.7	7	458	74
A41.5	Akasaka Limestone	Upper Member	109.5	21.4	18	501	32
A42.5	Akasaka Limestone	Upper Member	108.7	17.2	2	177	107
A43.5	Akasaka Limestone	Upper Member	107.9	22.6	2	112	55
A44.3	Akasaka Limestone	Upper Member	107.3	19.4	1	103	88
A44.8	Akasaka Limestone	Upper Member	106.9		1	35	73
A46.5	Akasaka Limestone	Upper Member	105.5	18.7	2	190	143
A48.5	Akasaka Limestone	Upper Member	103.9	21.0	7	500	79
A48.6	Akasaka Limestone	Upper Member	103.8	21.7	8	548	80
A49.1	Akasaka Limestone	Upper Member	103.4	18.2	23	801	41
A49.4	Akasaka Limestone	Upper Member	103.2	18.5	50	330	8
A49.8	Akasaka Limestone	Upper Member	102.9	18.9	31	760	28
A51.85	Akasaka Limestone	Upper Member	101.6	19.6	9	215	28
A54.9	Akasaka Limestone	Upper Member	101.2	16.3	11	754	79
A56.85	Akasaka Limestone	Upper Member	99.2	15.5	14	1092	90
A59.7	Akasaka Limestone	Upper Member	97.0	11.6	1	157	161
A63.5	Akasaka Limestone	Upper Member	93.9		1	81	163
A67.9	Akasaka Limestone	Upper Member	90.4	13.8	2	306	202
07AKA253	Akasaka Limestone	Upper Member	88.9	21.6	3	233	78
07AKA213	Akasaka Limestone	Upper Member	88.8		1	62	89
A74.4	Akasaka Limestone	Upper Member	85.2	13.3	2	106	70
07AKA207	Akasaka Limestone	Upper Member	82.0	22.5	10	1,123	130
A78.55	Akasaka Limestone	Upper Member	81.9		1	71	93
07AKA206	Akasaka Limestone	Upper Member	81.0	25.6	9	602	75
A82.65	Akasaka Limestone	Upper Member	78.6	22.3	1	192	158
06AKA50	Akasaka Limestone	Upper Member	77.2	24.1	19	1072	65
07AKA203	Akasaka Limestone	Upper Member	76.7	24.8	34	2,308	79
06AKA49	Akasaka Limestone	Upper Member	76.1	24.1	26	1,167	52
07AKA202	Akasaka Limestone	Upper Member	75.6	23.8	32	1,463	53
06AKA48	Akasaka Limestone	Upper Member	75.2	26.4	15	766	61
07AKA201	Akasaka Limestone	Upper Member	74.6	23.1	54	3,289	71
06AKA47	Akasaka Limestone	Upper Member	73.7	21.7	11	834	91

Table 2
Continued

Sample ID	Formation	Member	Thickness (m)	$\delta^{15}N_{acid.}$ (‰)	TN (ppm)	TOC (ppm)	C/N atomic
06AKA46	Akasaka Limestone	Upper Member	72.9	19.6	17	993	68
06AKA45	Akasaka Limestone	Upper Member	72.2	17.6	19	858	53
06AKA44	Akasaka Limestone	Upper Member	70.9	16.4	24	1,082	53
06AKA43	Akasaka Limestone	Upper Member	70.0	16.6	9	782	106
06AKA42	Akasaka Limestone	Upper Member	69.2	12.6	3	308	140
06AKA41	Akasaka Limestone	Upper Member	68.3	15.2	12	901	85
06AKA40	Akasaka Limestone	Upper Member	67.6	18.6	14	1,068	86
06AKA39	Akasaka Limestone	Upper Member	66.7	17.9	25	641	30
06AKA38	Akasaka Limestone	Upper Member	66.0	16.5	14	719	59
06AKA37	Akasaka Limestone	Upper Member	65.0	15.2	19	1,736	109
06AKA36	Akasaka Limestone	Upper Member	63.4	19.2	8	701	108
06AKA34	Akasaka Limestone	Upper Member	60.5	24.8	3	298	134
06AKA32	Akasaka Limestone	Upper Member	57.9	28.3	6	430	89
06AKA30	Akasaka Limestone	Upper Member	56.0	23.7	2	151	107
06AKA27	Akasaka Limestone	Upper Member	54.2	23.8	11	728	78
B2.4	Akasaka Limestone	Upper Member	54.1	25.2	7	550	89
06AKA26	Akasaka Limestone	Upper Member	52.9	25.1	2	152	88
06AKA24	Akasaka Limestone	Upper Member	51.3	22.7	14	1,083	92
06AKA23	Akasaka Limestone	Upper Member	51.0	21.7	7	522	85
B6.55	Akasaka Limestone	Upper Member	50.8	23.5	14	1,000	82
06AKA22	Akasaka Limestone	Upper Member	50.6	22.6	11	662	70
06AKA21	Akasaka Limestone	Upper Member	49.9	18.4	8	579	80
06AKA19	Akasaka Limestone	Upper Member	48.8	21.3	10	573	65
B10.15	Akasaka Limestone	Upper Member	47.9	21.3	2	206	97
B13.5	Akasaka Limestone	Upper Member	45.2	13.5	2	250	174
B16	Akasaka Limestone	Upper Member	43.2	12.2	3	406	144
B18.7	Akasaka Limestone	Upper Member	41.0	20.4	1	48	54
B22	Akasaka Limestone	Upper Member	38.4	19.8	25	710	33
B26.8	Akasaka Limestone	Upper Member	34.6	21.0	6	411	87
B28.8	Akasaka Limestone	Upper Member	33.0	16.4	3	50	20
B33.5	Akasaka Limestone	Upper Member	29.2	20.5	7	431	75
B34.2	Akasaka Limestone	Upper Member	28.6	16.5	16	2,065	151
B38.1	Akasaka Limestone	Upper Member	25.5	17.8	6	823	168
B43.9	Akasaka Limestone	Upper Member	20.9	21.6	7	199	33
B49.65	Akasaka Limestone	Upper Member	16.3	22.8	149	9,711	76
B53.6	Akasaka Limestone	Upper Member	13.1	17.9	9	953	120
B53.8	Akasaka Limestone	Upper Member	13.0	21.7	2	145	75
B57.5	Akasaka Limestone	Upper Member	10.0	18.0	7	668	106
B58.8	Akasaka Limestone	Upper Member	9.0	17.1	4	510	133
B61.4	Akasaka Limestone	Upper Member	6.9	19.2	3	293	119
B64	Akasaka Limestone	Upper Member	4.8	20.3	13	1,132	101
B64.9	Akasaka Limestone	Upper Member	4.1	21.6	12	1,256	119

Table 2
Continued

Sample ID	Formation	Member	Thickness (m)	$\delta^{15}N_{acid.}$ (‰)	TN (ppm)	TOC (ppm)	C/N atomic
B67.8	Akasaka Limestone	Upper Member	1.8	19.8	4	589	179
B69.5	Akasaka Limestone	Upper Member	0.4	21.3	15	245	19

Note. Record.

Moreover, the $\delta^{15}N_{acid.}$ values fluctuate largely and periodically in the analyzed succession, regardless of its consistent lithofacies (Kofukuda et al., 2014). No clear stratigraphic relationship between the fossil occurrence pattern and the $\delta^{15}N_{acid.}$ chemostratigraphy was recognized (Figure S1 in Supporting Information S1). An amplitude of the fluctuations is relatively small (ca. 2‰) in the lower part, and substantially increases up to eight‰ in the middle part. The amplitude then decreases upward and is ca. 5‰ in the uppermost part. The wavelet analysis shows the dominant cyclicity of approximately 16–32 m thickness in the middle to upper part of the analyzed limestone (Figure 6).

4.2. Model Results

All the model results are shown on Tables S7 and S8 in Supporting Information S1. In the local upwelling model, δ_{PON} in the surface box U is controlled by four factors: (a) R_U (the upwelling rate of deep-water from the box UM to U), (b) ΔO_2 (the redox condition in the open oceans, the boxes I and D), (c) δ_D (the $\delta^{15}N$ value of seawater nitrate in the deep-ocean box D), and (d) the presence or absence of nitrogen fixation in the surface ocean box U (Figure 2). For the last factor, we considered two cases: one in which nitrogen fixation is limited in box U ("non-N-fixation case"), and the other in which nitrogen fixation is not limited in box U ("N-fixation case") (Boyle et al., 2013).

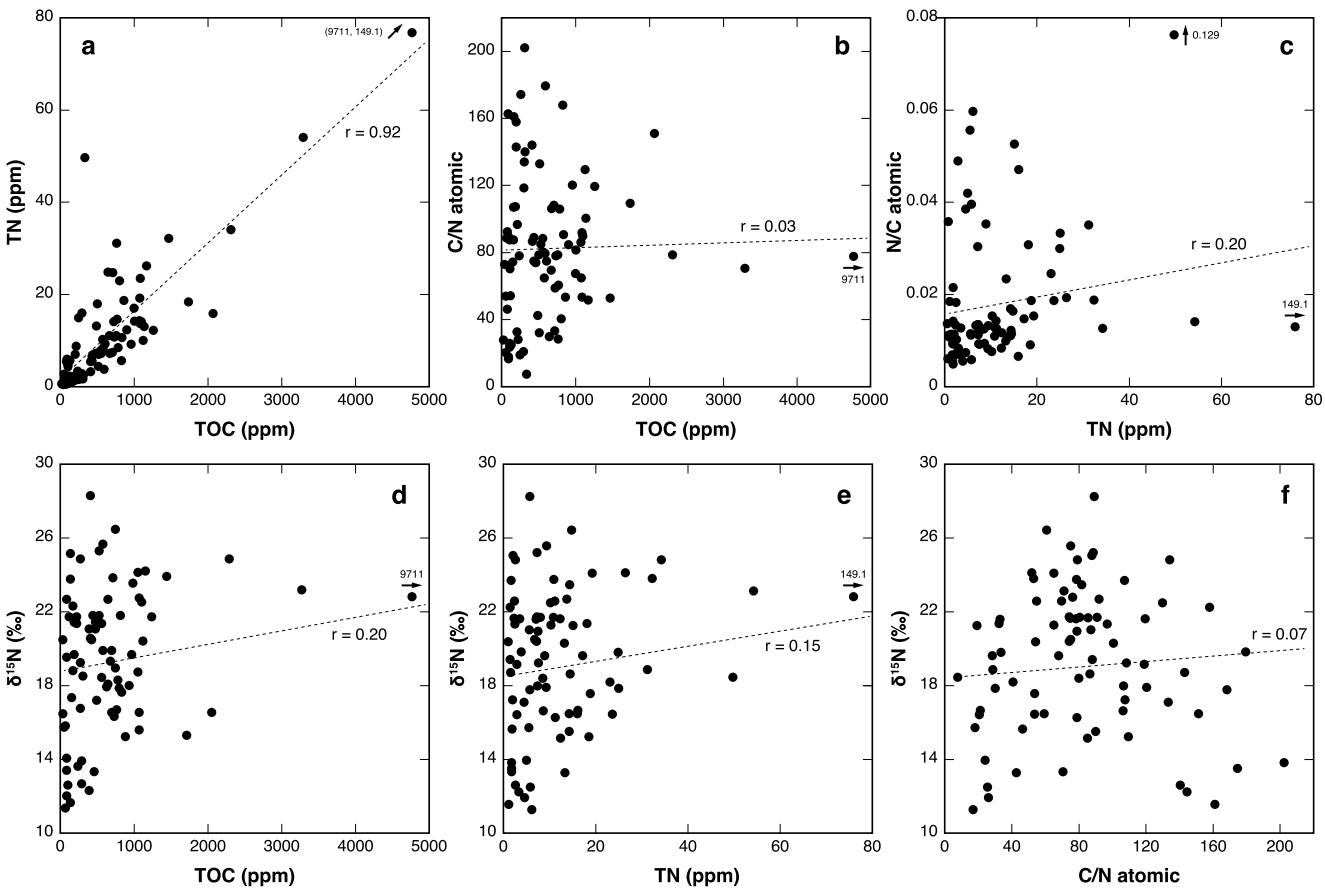

Figure 4. Geochemical cross plots of the Akasaka data.

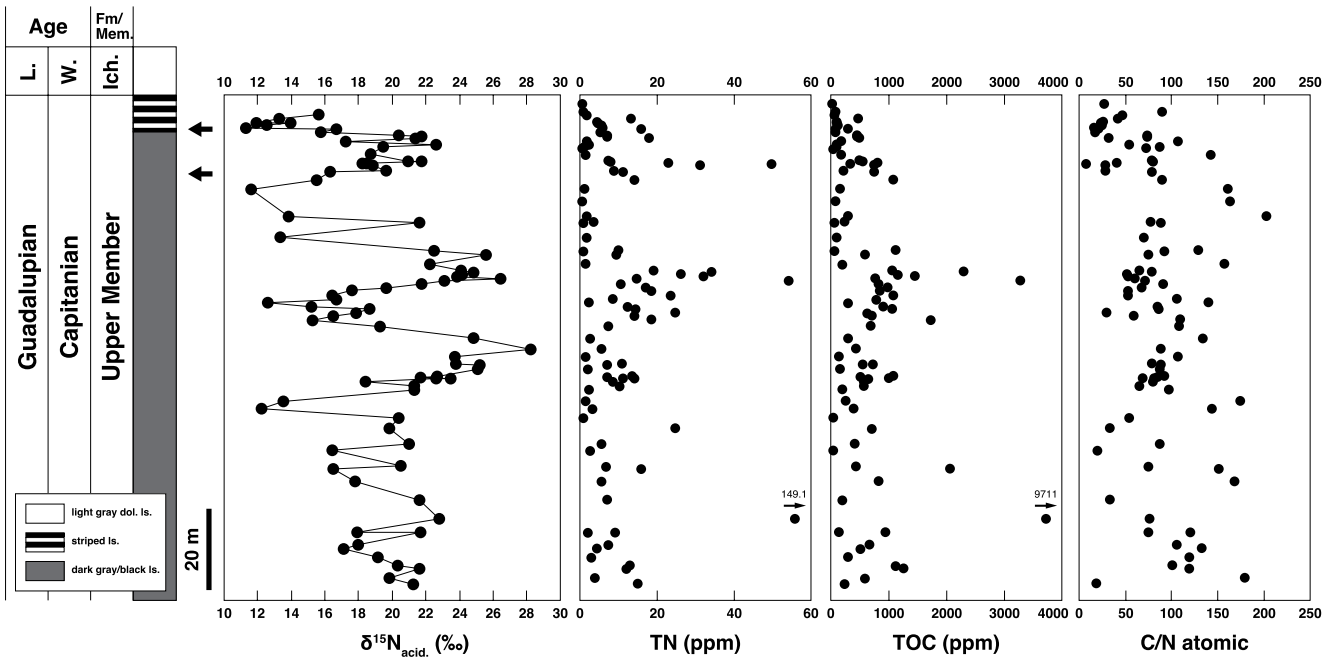

Figure 5. Chemostratigraphy of the Akasaka limestone. Two major extinction horizons are shown by arrows (Kofukuda et al., 2014). L.: Lopingian, W.: Wuchiapingian, Ich.: Ichihashi Formation, TN: total nitrogen, TOC: total organic carbon.

4.2.1. Non-N-Fixation Case

Figure 7a shows the concentration of chemical species in the box UM at the standard oceanic condition ($\Delta O_2 = 0$ μM), when nitrogen fixation is limited in box U. Figure 7b shows the rate of export production (*EP*), denitrification (R_{deni}), and sulfate reduction (R_{MSR}) in the box UM at the standard condition. At the standard oceanic condition with no nitrogen fixation in box U, the O_2 and NO_3^- concentrations in the box UM decreases and increases, respectively, with the upwelling rate R_U for up to 0.18 cm/hr (Figure 7a; Table S6 in Supporting Information S1). This is due to the increase in the rate of aerobic respiration and subsequent nitrification in UM. When R_U is higher than 0.18 cm/hr, O_2 supplied from the boxes U, I, and D to the box UM is completely consumed by aerobic respiration and denitrification occurs. The rate of denitrification and the NO_3^- concentration in the box UM ($NO_3^-{}_{,UM}$; "NO_3^-" in Figure 7a) increases and decreases, respectively, with R_U (Figures 7a and 7b). However, the slope of $\Delta NO_3^-{}_{,UM}/\Delta R_U$ decreases with R_U and NO_3^- in the box UM is not completely consumed when the box UM becomes apparently O_2-depleted. This is because a negative feedback mechanism works between the denitrification and export production, that is, the nitrogen limitation for primary production in box U (Table A2). The relationships among the O_2 and NO_3^- concentrations in the box UM and the export production from box U to UM in the present model are consistent with the spatial distribution of O_2 and NO_3^- in mid-depth waters within and around the Peruvian ODZ in the eastern tropical South Pacific (e.g., Peters et al., 2018). See Note 3 in Appendix A for more details.

Figure 7c shows the δ_{PON} dependency on R_U at the standard oceanic condition. δ_{PON} increases with R_U due to the enhanced input of ^{15}N-enriched nitrate and ammonium from the box UM to U via upwelling (Figure 7c). However, the slope of $\Delta\delta_{PON}/\Delta R_U$ decreases with R_U because primary productivity in box U is limited by upwelled fixed-N and nitrate is not completely consumed in the box UM (Figure 7a).

As well as R_U, ΔO_2 is also an important controlling factor of δ_{PON} (Figure S2 in Supporting Information S1). For a typical example, at the standard oceanic condition, the Akasaka $\delta^{15}N$ range cannot be fully covered at any given δ_D (Figure 7). Our calculations show that, within the present R_U range (0–2.0 cm/hr) (Boyle et al., 2013; Canfield, 2006), the Akasaka $\delta^{15}N$ range can be fully covered only when ΔO_2 is <−80 μM (Figures 8a and 8b). The possible range of ΔO_2 and δ_D on which the Akasaka $\delta^{15}N$ range is fully covered is shown as a red line/parallelogram in Figure 8b. The line/parallelogram is enclosed by the black polyline on which the maximum δ_{PON} is +28‰ and by the gray polyline on which the minimum δ_{PON} is +11‰. In the present modeling, as mentioned in Section 3.3.1, we assumed complete assimilation of upwelled nitrate and ammonium and thus no nitrogen isotope fractionation via assimilation in box U (Section 3.3.1). However, in some areas in the modern surface oceans,

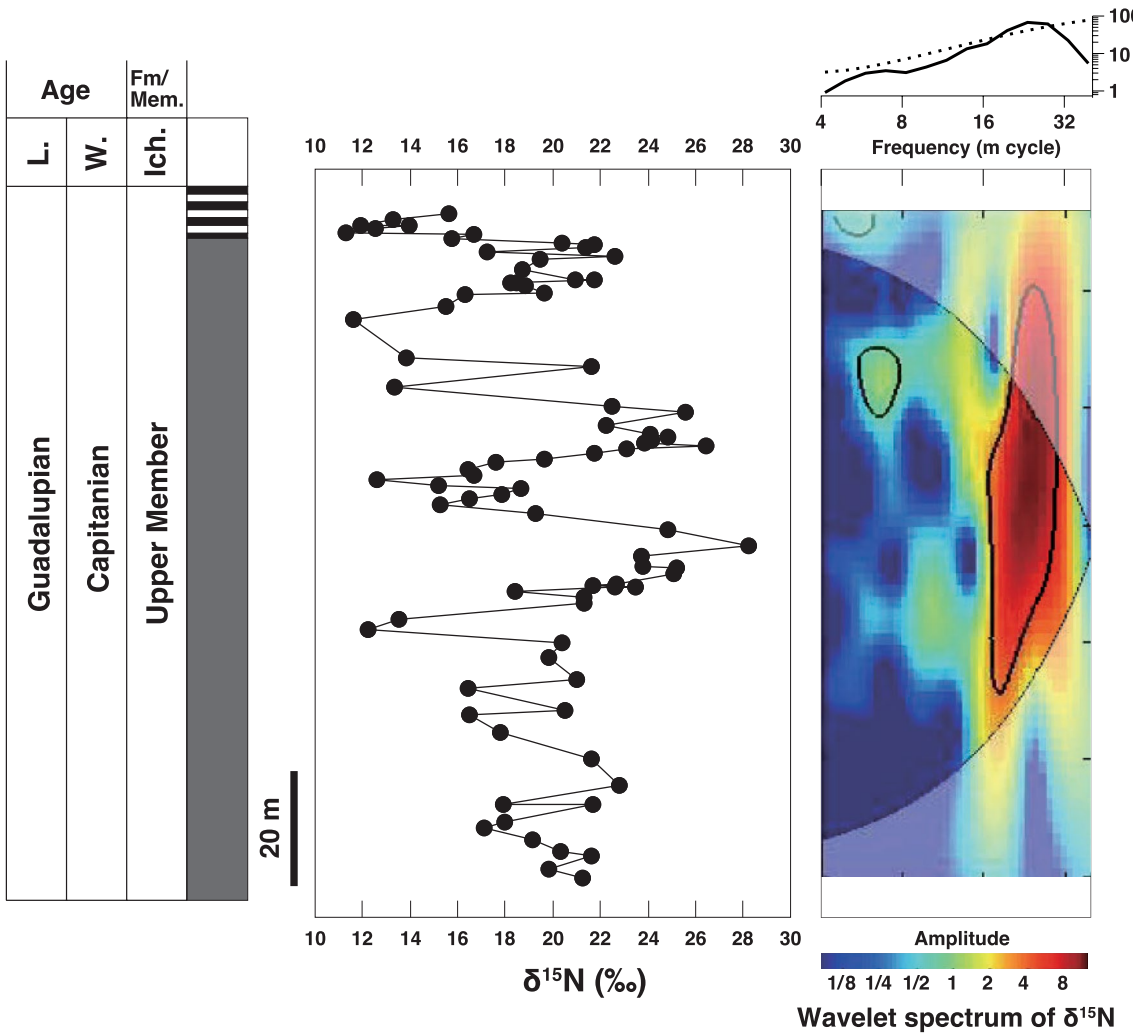

Figure 6. The wavelet spectra and whole section power spectra (Torrence & Compo, 1998) of the Akasaka $\delta^{15}N_{acid.}$ record. Legends of lithology are same as in Figure 1e. Pale area delineates cone of influence, within which wavelet power is uncertain. Black contour is the 90% confidence level, using a red-noise (autoregressive lag 1) background spectrum (Torrence & Compo, 1998).

partial assimilation of nitrate with the nitrogen isotope fractionation of ~5‰ due to iron limitation for primary production is observed (e.g., Altabet, 2001; Sigman and Fripiat, 2019; Wada, 1980).

Considering the uncertainty of the potential nitrogen isotope fractionation via fixed-N assimilation on the Akasaka $\delta^{15}N_{acid.}$ record, in the present modeling, we focused solely on the possible maximum ΔO_2 and minimum δ_D on which the Akasaka $\delta^{15}N_{acid.}$ range (+11‰ to +28‰) is fully covered. As discussed later, the estimation of the possible maximum ΔO_2 and minimum δ_D corresponds to that of the most potentially oxidizing condition in the Capitanian ocean. Although the possible range of ΔO_2 and δ_D on which the Akasaka $\delta^{15}N$ range is fully covered is on the red line or in the red parallelogram in Figure 8b, our estimation in this study allows that ΔO_2 and δ_D in the Capitanian ocean were in the gray area in Figure 8b. With the supposed constraint on δ_I (δ_D −2‰ ≤ δ_I ≤ δ_D +2‰), the possible maximum ΔO_2 and minimum δ_D were especially achieved when δ_I was δ_D +2‰ (the right figure in Figure 8b). We therefore estimated that the possible maximum ΔO_2 and minimum δ_D in the Capitanian ocean were −80 μM and +9‰, respectively.

4.2.2. N-Fixation Case

Figure 7d shows the concentration of chemical species in the box UM at the standard oceanic condition (ΔO_2 = 0 μM), when nitrogen fixation is not limited in box U. Figure 7e shows the rate of export production (EP), denitrification (R_{deni}), and sulfate reduction (R_{MSR}) in the box UM and of nitrogen fixation (F_{Nfix}) in box

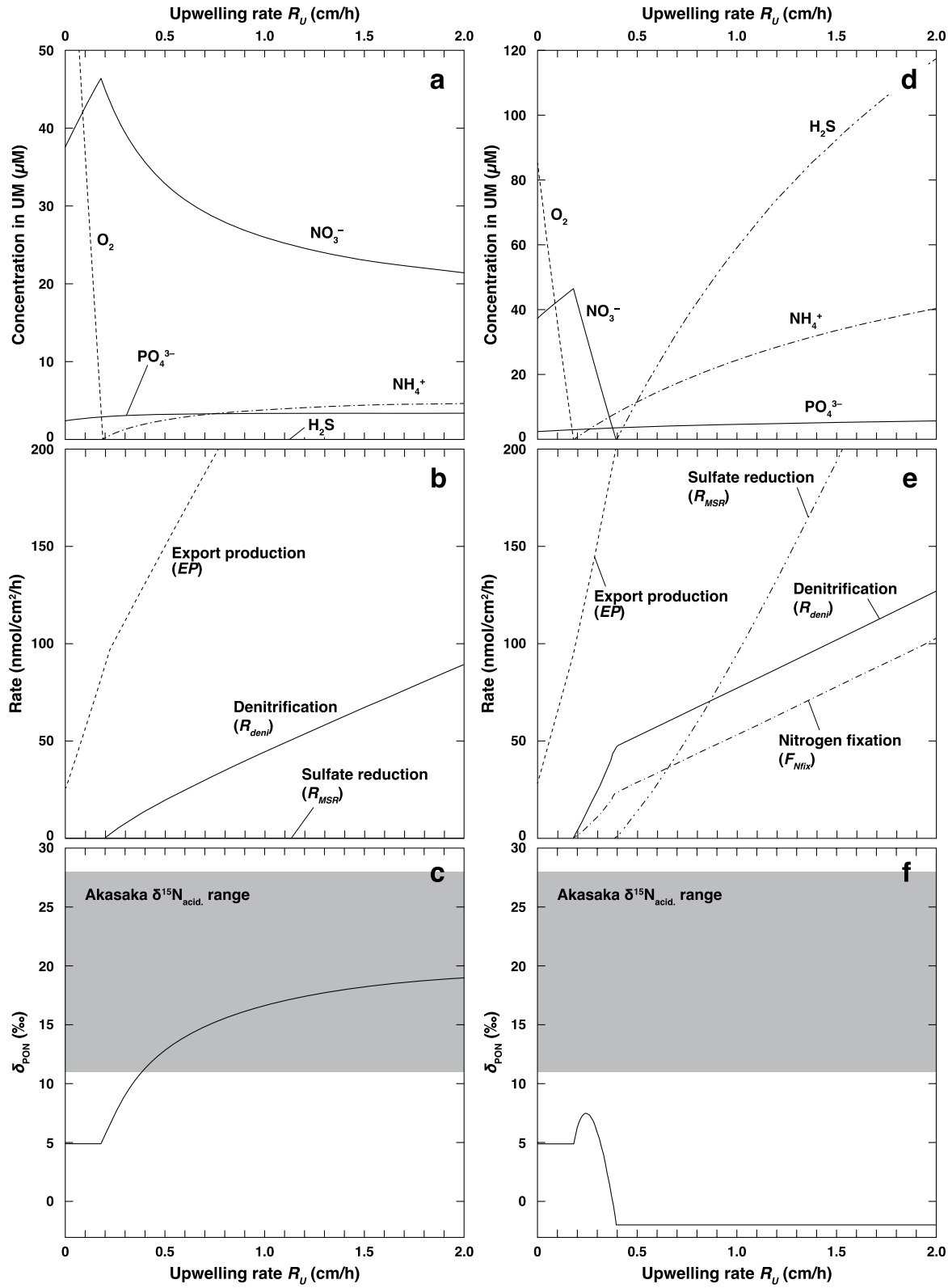

Figure 7.

U at the standard condition. Figure 7f shows the δ_{PON} dependency on R_U. At the standard oceanic condition, O_2 is completely consumed and anaerobic respiration occurs in the box UM when R_U is higher than 0.19 cm/hr (Figure 7d; Table S6 in Supporting Information S1), as in the non-N-fixation case (Figure 7a). When R_U is higher than 0.19 cm/hr, denitrification and nitrogen fixation occur in the box UM. In the range of R_U from 0.19 cm/hr to 0.40 cm/hr, the input of ^{15}N-enriched nitrate and ammonium from the box UM tends to increase δ_{PON} with R_U, while nitrogen fixation supplies ^{15}N-depleted ammonium into box U and suppresses the δ_{PON} increase with R_U (Figure 7f). Primary productivity in the surface box U is limited by upwelled phosphate (PO_4^{3-}) (Figure 7d). When R_U is higher than 0.4 cm/hr, nitrate in the box UM is completely consumed via denitrification and δ_{PON} is constantly −2‰ because nitrogen fixation is the only nitrogen source for PON in box U. In the N-fixation case, the Akasaka $\delta^{15}N_{acid.}$ range (+11‰ to +28‰) cannot be fully covered at any given ΔO_2 and δ_D because δ_{PON} does not reach +28‰ due to nitrogen fixation in box U (Figures 7f and 8c). Our results are generally consistent with those in Boyle et al. (2013), in which an euxinic water-mass emerges in the box UM when nitrogen fixation is not limited and sustains biological productivity in the surface box U (Figure 7d).

5. Discussion

5.1. Preservation of the Original Isotopic Composition

5.1.1. The δ^{15}N Record of Surface-Ocean PON Around the Seamount Top

Geochemical cross plots are useful to constrain the nitrogen source for the analyzed Akasaka limestone (Figure 4). The TN and TOC contents are positively correlated (Figure 4a), suggesting that the direct nitrogen source for the limestone is mainly sedimentary organic matter. All of the analyzed rocks are fresh and pure bioclastic limestone with no land plant debris nor aerial dust observed under microscope (Kofukuda et al., 2014). Moreover, no clear correlation is recognized between the $\delta^{15}N_{acid.}$ value and the C/N ratio (Figure 4f). The δ^{15}N value and C/N ratio of land plants are generally lower and higher, respectively, than those of marine algae (Meyers, 1994; Peters et al., 1978). No correlation between $\delta^{15}N_{acid.}$ and C/N at Akasaka does not support an input of terrestrial nitrogen source and its mixing with a marine source. The $\delta^{15}N_{acid.}$ value of the Akasaka limestone likely records the δ^{15}N value of marine PON at the top of the seamount ($\delta^{15}N_{PON}$) in the Capitanian. $\delta^{15}N_{PON}$ corresponds to δ_D in the local upwelling model (Figure 2).

5.1.2. The Influence of Post-Depositional Alteration

The C/N atomic ratio of living marine organism is generally around 6.6, the Redfield ratio. The relatively high C/N ratios (up to 200) of the Akasaka limestone suggest nitrogen losses after burial (Figures 4b and 5). When the sediments sustain thermal maturation, their TOC contents and C/N ratios would decrease and increase, respectively, showing a negatively-correlated variation between the TOC content and the C/N ratio (e.g., Bristow et al., 2009). No correlation between the TOC and C/N ratio at Akasaka implies that the grade of thermal maturity is not high. During early diagenesis, the δ^{15}N value of sedimentary organic matter would increase by a selective ^{14}N loss (e.g., Altabet & Francois, 1994; Jia & Kerrich, 2004; Robinson et al., 2012; Williams et al., 1995), producing a negatively-correlated variation between the δ^{15}N value and the TN content (e.g., Cremonese et al., 2013); that is not the Akasaka case (Figure 4e). We therefore conclude that diagenetic thermal maturation of sedimentary organic matter is not significant at Akasaka (cf., Martínez-García et al., 2022).

5.1.3. The Influence of Pre-Measurement HCl Rinse

In the pre-measurement procedure, we removed carbonate in the analyzed limestone by the reaction with HCl ('rinse method'; Brodie et al., 2011), due to the low TN and TOC contents of the analyzed rocks (Table 2). Previous studies reported that the bulk δ^{15}N value of sediments can be altered by HCl rinse, possibly due to losses of nitrogen in clay minerals and/or acid soluble organic matter (Brodie et al., 2011; Fujisaki et al., 2021; Schlacher

Figure 7. Model results at the standard oceanic condition ($\Delta O_2 = 0$ μM) with δ_I and δ_D of +4.9‰ (the default value; Table A1). (a)–(c) The "non-N-fixation case" in which nitrogen fixation is limited in the surface ocean box U. (a) Chemical species in the box UM (b) The rate of export production (*EP*) from box U to UM and of denitrification (R_{deni}) and sulfate reduction (R_{MSR}) in the box UM. See Appendix B for their derivation. (c) The dependency of δ_{PON} of box U on the upwelling rate of deep-water (R_U). Also see Table A2. The Akasaka δ^{15}N range (light gray area) is not fully covered at the standard oceanic condition. (d)–(f) The "N-fixation case" in which nitrogen fixation is not limited in U. (d) Chemical species in UM. (e) The rate of export production from U to UM (*EP*), of nitrogen fixation in U (F_{Nfix}), and of denitrification and sulfate reduction in UM (R_{deni} and R_{MSR}, respectively). See Appendix B for their derivation. (f) The dependency of δ_{PON} on R_U (derived from Equation A18 in Appendix B. Also see Table A2. The Akasaka $\delta^{15}N_{acid.}$ range cannot be covered in the N-fixation case. Numerical modeling data are shown on Table S6 in Supporting Information S1.

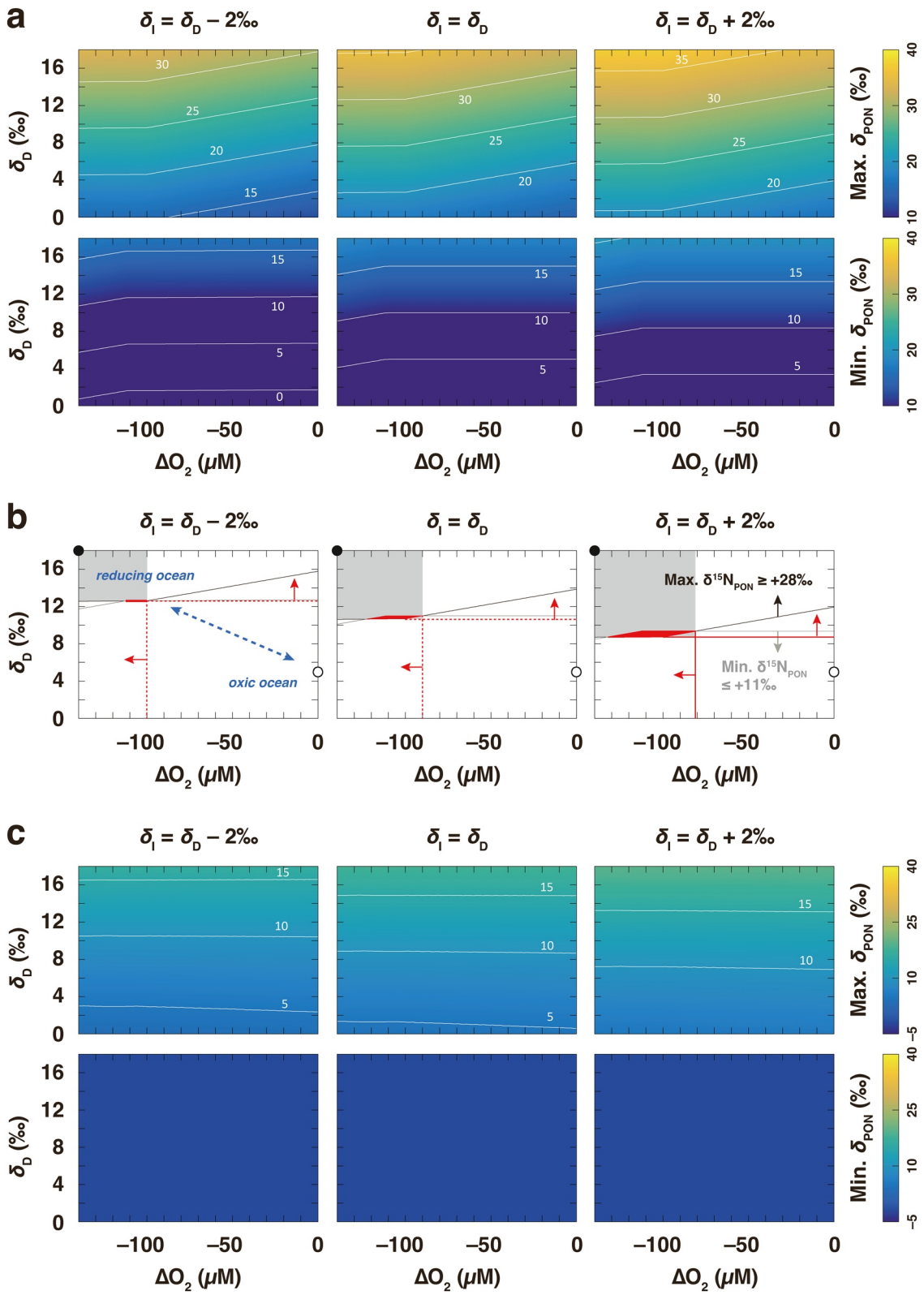

Figure 8.

and Connolly, 2014). A compilation of $\delta^{15}N$ changes via HCl rinse at room temperature (similar to in the present study) in previous studies shows that the magnitude of $\delta^{15}N$ changes (the difference between the $\delta^{15}N$ value after HCl rinse ($\delta^{15}N_{acidified}$) and the value before HCl rinse ($\delta^{15}N_{untreated}$); $\delta^{15}N_{acidified} - \delta^{15}N_{untreated}$) mostly ranges from −2‰ to +1‰ (Table S5 in Supporting Information S1). We regarded this magnitude of $\delta^{15}N$ changes (−2‰ to +1‰) reported in previous studies as the potential $\delta^{15}N$ changes of our samples via HCl rinse.

Based on these potential $\delta^{15}N$ changes of our samples (−2‰ to +1‰), we considered the potential uncertainty of the estimation of the possible maximum ΔO_2 and minimum δ_D in the Capitanian ocean (Figure 8). As mentioned in Section 4.2.1, we estimated that the possible maximum ΔO_2 and minimum δ_D in the Capitanian ocean were −80 μM and +9‰, respectively (the right figure in Figure 8b), based on the present Akasaka $\delta^{15}N$ record and the local upwelling model. While the potential $\delta^{15}N$ changes of the analyzed samples via HCl rinse would directly affect the estimate of δ_D, it would not affect the estimate of ΔO_2 in the present modeling (Text S3 in Supporting Information S1). Considering the potential $\delta^{15}N$ changes via HCl rinse as the potential uncertainty of the estimated δ_D in the Capitanian ocean, we concluded that the possible maximum ΔO_2 and minimum δ_D in the Capitanian ocean were −80 μM and +9 + 2/–1‰, respectively.

5.2. The Substantially High $\delta^{15}N_{acid.}$ Value of the Akasaka Limestone

5.2.1. High $\delta^{15}N_{NO3}$ Value in the Reducing Ocean

The Akasaka limestone is characterized by the substantially high $\delta^{15}N_{acid.}$ values (+19.4‰ on average) (Figure 5). In Earth history, stratigraphic records with high $\delta^{15}N$ value over +20‰ had been reported only from a sedimentary succession in the 2.7 Ga Tumbiana Formation (Stüeken et al., 2015; Thomazo et al., 2011) and in the 2.0 Ga Aravalli Supergroup (Papineau et al., 2009). Those Neoarchean and Paleoproterozoic strata accumulated in restricted water environments (e.g., Awramik & Buchheim, 2009; Buick, 1992; Roy & Paliwal, 1981; Sakurai et al., 2005; Thorne & Trendall, 2001) under basically anoxic conditions with local redox variation due to in situ oxygenic photosynthesis on oxygen-depleted Precambrian Earth (Nishizawa et al., 2010; Papineau et al., 2009; Yoshiya et al., 2012). Although key processes in the nitrogen cycle in the reducing early hydrosphere are still debated, the fractional loss of dissolved ammonium (microbial conversion to N_2 via nitrification coupled to denitrification and/or abiotic devolatilization at high pH) could have contributed to the high $\delta^{15}N$ value of a local ammonium reservoir in the restricted environments recorded in those Precambrian strata (Papineau et al., 2009; Stüeken et al., 2015; Thomazo et al., 2011). In marked contrast, the present Akasaka limestone accumulated in the pelagic surface ocean in mid-Panthalassa in the oxygenated Phanerozoic ocean-atmosphere system ($pO_2 = \sim 20\%$, Berner, 2006), and thus should have recorded, at least in part, the $\delta^{15}N$ value of nitrate in the deep-water of the open ocean. (See Text S4 in Supporting Information S1 for more details.)

As discussed in Section 5.1, the $\delta^{15}N_{acid.}$ value of the Akasaka limestone likely records the value of marine PON at the top of the seamount in the Capitanian. To fully cover the Akasaka $\delta^{15}N_{acid.}$ range (+11‰ to +28‰) in the supposed R_U range between 0 cm/hr and 2.0 cm/hr (Canfield, 2006), the present local upwelling model requests the substantially reducing oceanic condition on a global scale ($\Delta O_2 \leq -80$ μM) and the high $\delta^{15}N$ value of seawater nitrate in the deep ocean (δ_D) (≥+9‰) when nitrogen fixation was limited in the surface water around the seamount ("non-N-fixation case") (Figures 8a and 8b). Based on the model results of the N-fixation case (Section 4.2.2), it was most likely that nitrogen fixation was consistently limited in the surface water around the seamount top in mid-Panthalassa (Figure 6f).

As mentioned in Section 3.3.2, δ_D in the local upwelling model (Figure 2) corresponds to $\delta^{15}N_{NO3}$, the $\delta^{15}N$ value of an oceanic nitrate reservoir, in the global isotope mass balance (Figure 3). Capitanian $\delta^{15}N$ records are few, but shelf sediment records at Opal Creek, Alberta, and at Chaotian, South China, are consistent with the high

Figure 8. The maximum and minimum δ_{PON} as a function of ΔO_2 and δ_D within the supposed range of R_U (0 cm/hr to 2 cm/hr) in the local upwelling model. (a) Non-N-fixation case. (b) The possible range of ΔO_2 and δ_D on which the Akasaka $\delta^{15}N_{acid.}$ range is fully covered (red line/parallelogram) in the non-N-fixation case. The red line/parallelogram is enclosed by the black polyline on which the maximum δ_{PON} is +28‰ and by the gray polyline on which the minimum δ_{PON} is +11‰. A black arrow indicates the area in which the maximum δ_{PON} is higher than +28‰ whereas a gray arrow indicates the area in which the minimum δ_{PON} is lower than +11‰. Red arrows indicate the range of possible values of ΔO_2 and δ_D, respectively, in the Capitanian ocean. We estimated the possible maximum ΔO_2 and minimum δ_D by the modeling, and thus ΔO_2 and δ_D in the Capitanian ocean should have been in the gray area in each figure. White and black dots represent the modern and "nitrogenous" oceans, respectively (Figure 3b). Note that δ_D (the $\delta^{15}N$ value of seawater nitrate in the deep-ocean box D) in the upwelling model corresponds to $\delta^{15}N_{NO3}$ (the $\delta^{15}N$ value of a global deep-oceanic nitrate reservoir) in the global nitrogen isotope mass balance. (c) N-fixation case. The Akasaka $\delta^{15}N_{acid.}$ range cannot be fully covered in this case.

$\delta^{15}N_{NO3}$ value (Figure 1). Schoepfer et al. (2012) reported the relatively high $\delta^{15}N$ values up to +10‰ of the Guadalupian Ranger Canyon Fm at Opal Creek in NW Pangea, though the G–LB interval is lacking due to a large unconformity. Saitoh et al. (2014) analyzed the $\delta^{15}N$ value of Capitanian carbonates/mudstones of deep-water facies accumulated on the relatively deep slope/basin at Chaotian in the low-latitude easternmost Tethys. They found the substantially high $\delta^{15}N$ values up to +14‰ in the early to middle Capitanian and attributed them to enhanced denitrification in an anoxic deep-water mass. Although the unconformities around the G–LB in both sections prevent their exact chemostratigraphic correlation, it is worth noting that these two sections were located almost on the opposite side of the globe from each other (Figure 1a). Their geographical relationship implies that organic matter with high $\delta^{15}N$ value (>10‰) was produced on a global scale in the Capitanian shallow oceans, and that is consistent with the high $\delta^{15}N_{NO3}$ value (≥+9‰) inferred from the mid-Panthalassic Akasaka record. Nonetheless, the high oceanic $\delta^{15}N_{NO3}$ value in the model is inconsistent apparently with relatively low $\delta^{15}N$ values (0 to +2.5‰) of pelagic sediments in western Panthalassa, which is now exposed as an allochthonous block at Gujo-Hachiman in southwest Japan (Fujisaki et al., 2019), although the Gujo-Hachiman shale/chert, as well as the Akasaka limestone, accumulated originally in mid-Panthalassa. We infer that the low $\delta^{15}N$ values of the deep-sea shales do not record the $\delta^{15}N$ value of the oceanic nitrate reservoir but reflect a contribution of ^{15}N-depleted organic matter produced via regional nitrogen fixation in the N-scarce pelagic surface water and/or of ^{15}N-depleted terrestrial ammonium/organic matter trapped in aeolian clay to the abyssal sediments.

5.3. The Redox Structure of the Capitanian Ocean

Based on the Akasaka $\delta^{15}N_{acid.}$ record and the local upwelling model, we estimated that the possible maximum ΔO_2 and minimum δ_D in the Capitanian ocean were −80 μM and +9 + 2/–1‰, respectively (Figure 8). We then constrained the global redox structure of the Capitanian ocean based on two different approaches. These two approaches are based on each of the constrained maximum ΔO_2 and minimum δ_D (i.e., $\delta^{15}N_{NO3}$) in the Capitanian ocean, respectively.

5.3.1. The Redox State of Panthalassic Deep-Waters

Based on the possible maximum ΔO_2 (−80 μM) in the local upwelling model (Figure 2), $O_{2,I}$ and $O_{2,D}$ are estimated to be less than 20 μM and less than 60 μM, respectively. In particular, the estimated maximum $O_{2,D}$ (60 μM) is in the range of the "dysoxic zone" (~10 μM < O_2 < ~100 μM) according to the aqueous redox classification (Algeo & Li, 2020; Tyson & Pearson, 1991).

Isozaki (1997) proposed that the deep part of the Panthalassic ocean was under prolonged anoxic conditions from the Capitanian to the Early Triassic (superanoxia), on the basis of petrological observations of deep-sea cherts incorporated into accretionary complexes in Japan and British Columbia, Canada (Figure 1d). Nevertheless, the detailed redox state of mid-Panthalassic deep-waters in the Capitanian stage based on petrological/geochemical studies on the pelagic sediments from the superocean has been controversial (Isozaki, 2009a, 2014; Kakuwa, 2008; Kato et al., 2002; Matsuo et al., 2003). Fujisaki et al. (2019) reported no authigenic enrichment of molybdenum (Mo) and uranium (U) in mid-Panthalassic deep-sea claystone interbedded with chert in central Japan and suggested pervasive oxic conditions on an abyssal plain in the Capitanian. Onoue et al. (2021) recently reported manganese (Mn) depletion (relative to lithogenic background) in claystone from another allochthonous chert block in Japan, and concluded that the deep waters were predominantly suboxic (0 μM < O_2 < ~10 μM; Tyson & Pearson, 1991; Algeo & Li, 2020) in the stage.

According to the redox classification (Algeo & Li, 2020), the suboxic zone is characterized by several redox couples including MnO_2/Mn^{2+} and $UO_2(OH)_2/UO_2$ while the euxinic zone is characterized by the MoO_4^{2-}/MoS_4^{2-} couple. Assuming that redox reactions of these metals occurred only in the water column, no enrichment of Mn, U, and Mo in the analyzed pelagic sediments may suggest that, in the Capitanian, the Panthalassan deep-waters were in the narrow redox window in the suboxic zone in which only Mn is reduced (Onoue et al., 2021). However, the redox reaction of transition metals is a common biogeochemical process not only in the water column but also in the surface sediments (e.g., Algeo & Li, 2020; Tribovillard et al., 2006). In the modern OMZs along the continental margins, sediments overlain by the suboxic waters are commonly depleted in Mn (e.g., Böning et al., 2004; Borchers et al., 2005; Nameroff et al., 2002). This is because particulate Mn (hydr)oxides are reduced to soluble Mn^{2+} in the reducing water-column and sediments (e.g., Froelich et al., 1979; Nameroff et al., 2002). It is worth noting that, even when the sediments are overlain by the dysoxic water, soluble Mn^{2+} in the sediment porewater

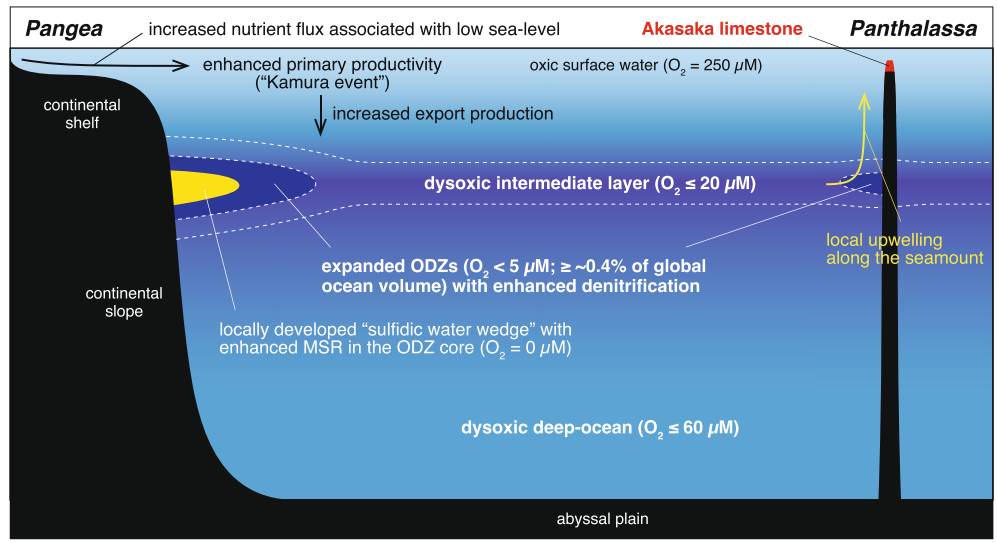

Figure 9. The redox structure of the Capitanian superocean (not to scale). The oxic surface water (O_2 = 250 μM) is a model assumption (Canfield, 2006). MSR: microbial sulfate reduction, ODZ: oxygen-deficient zone.

would escape to the overlying water by diffusion (e.g., Böning et al., 2004; Johnson et al., 1992; McManus et al., 2012; Morford & Emerson, 1999). Hence, Mn depletion in sedimentary records may not be a robust indicator of bottom-water suboxia in the past ocean.

Furthermore, modern sediments overlain by the suboxic water are generally enriched in U and Mo because their reduction and authigenic fixation are promoted within the more reducing sediment porewaters (e.g., Böning et al., 2004; Borchers et al., 2005; Nameroff et al., 2002). However, the Capitanian Panthalassic pelagic sediments are not enriched in U and Mo (Fujisaki et al., 2019; Onoue et al., 2021). Considering the vertical redox gradient in the water column and sediments, no authigenic enrichment of U and Mo in the analyzed sediments may not be indicative of the suboxic deep-water on a mid-Panthalassic abyssal plain. As illustrated above, it is difficult to distinguish the redox state of bottom water from that of sediment porewater based especially on the depletion (or no authigenic enrichment) of redox-sensitive metals in the pelagic sediments.

Apart from this essential difficulty in the "bottom-up" approaches, the present shallow-marine $\delta^{15}N_{acid.}$ record of the Akasaka limestone with global oceanographic modeling does not require that the Panthalassic deep-ocean was predominantly suboxic (O_2 < ~10 μM) in the Capitanian, but allows that the deep-ocean was dysoxic (O_2 ≤ 60 μM) (Figure 9). We emphasize the utility of such a "top-down" approach to constrain the average deep-water redox condition on a global scale in the past ocean. The dysoxic large deep-oceans in the Capitanian are supported by a U isotope record from shelf carbonates. Based on the U isotopic composition of carbonates in South China during the Permian–Triassic transition, Elrick et al. (2017) suggested that the seafloor areas overlain by anoxic/euxinic waters were not widespread in the Capitanian oceans although only one datum was reported from the stage.

5.3.2. The Minimum Volume of Expanded ODZs Along the Continental Margins

As the second approach to the reconstruction of the redox structure of the Capitanian ocean, we estimated the volume of ODZs on a global scale from the *f* value (in the global isotope mass balance) of the Capitanian ocean. The Akasaka $\delta^{15}N_{acid.}$ record suggests that δ_D in the local upwelling model was ≥ +9‰ in the Capitanian ocean (Section 5.3.1). δ_D corresponds to the $\delta^{15}N_{NO3}$ value in the global isotope mass balance (Figure 3a), and the $\delta^{15}N_{NO3}$ value correlates linearly with the *f* value (Figure 3b). The estimated *f* value of the Capitanian ocean from Equation A9 is substantially high (≥0.5) compared to of the modern oceans (0.27) (Figure 3b), and suggests the enhanced water-mass denitrification in the expanded ODZs at intermediate water depths in the Capitanian ocean (Figure 9).

Based on the constrained minimum *f* value (0.5), we estimated the possible minimum volume of the ODZs on a global scale in the Capitanian ocean with three simple assumptions as follows. First, the $\delta^{15}N$ value and size

of a global oceanic nitrate reservoir were constant during the stage. (It is the assumption of the nitrogen isotope mass balance in the ocean.) Second, the volumetric rate of water-column denitrification in the Capitanian ODZ was identical to that in the modern ODZ. Finally, a global flux of sedimentary denitrification in the Capitanian ocean was identical to that in the modern oceans. Given that the present ODZs constitute 0.2% of global ocean volume (Bianchi et al., 2012) and that denitrification in the modern ODZs is responsible for 27% of fixed-N loss from the oceans (Galloway, 2014; Robinson et al., 2012), we estimated that the ODZs expanded to ∼0.5% of global ocean volume in the Capitanian at the minimum, at the given $\delta^{15}N_{NO3}$ of +9‰ (Text S6 and Table S9 in Supporting Information S1). Even when the uncertainty of estimated minimum $\delta^{15}N_{NO3}$ (according to the potential $\delta^{15}N$ changes of the analyzed rocks via HCl rinsing) is considered ($\delta^{15}N_{NO3} = \delta_D$ = +9 +2/–1‰), the ODZs constituted ∼0.5 +0.3/–0.1% of global ocean volume at the minimum in the ocean. Hence, the volume of ODZs in the Capitanian ocean was at least twice as much as in the modern oceans.

The expanded ODZs in the reducing Capitanian ocean, suggested by the present Akasaka record and models, are in agreement with a growing body of geologic evidence for prevailing anoxic/sulfidic waters along continental margins in South China (Kametaka et al., 2005; Saitoh et al., 2013a, 2014a; Shi et al., 2016; Wei et al., 2016, 2019; B. Zhang et al., 2018, 2019a, 2021; G.J. Zhang et al., 2015), NW Pangea (Bond et al., 2020; G.J. Zhang et al., 2015), and the Boreal Realm (Bond et al., 2015) (Figure 1a). Based on those observations, Saitoh et al. (2014a, 2017) proposed an episode of ODZ expansion in the Capitanian ocean with the emergence of a "sulfidic water wedge" along the continental margin (Figure 9). In the modern oxic oceans, a sulfidic water plume episodically emerges in the ODZ core on a eutrophic shallow shelf and disappears within a month due to quick sulfide oxidation (Lavik et al., 2009; Schunck et al., 2013). In contrast, in the Capitanian reducing oceans, the sulfidic water masses were likely developed along the deeper continental margins and persisted for >1 Myr (Saitoh et al., 2014). The Capitanian oceans are characterized by increased marine primary productivity and export production based on the high $\delta^{13}C$ value of carbonate (>+5‰) on a global scale, associated possibly with climate cooling (Kamura event; Isozaki et al., 2007a, 2007b, 2011). The substantially low sea-level associated with limited coastal shelf areas in the Capitanian may have contributed to increased phosphorous flux to the open ocean, thereby stimulating the primary production (Algeo et al., 2014; Ozaki & Tajika, 2013), and to the development of the sulfidic water-bearing ODZs along the continental margins rather than on the shallow shelves in the Capitanian (Figure 9). The enhanced open-ocean productivity with high export production may also have resulted in the globally reducing Capitanian oceans ($\Delta O_2 \leq -80$ μM) in which the sulfidic water masses within the expanded ODZs persisted ∼10^7 times longer compared to in the modern oceans.

In summary, we estimated the global redox structure of the Capitanian superocean based on two different approaches. The two approaches are based on the maximum ΔO_2 and minimum δ_D (i.e., $\delta^{15}N_{NO3}$) in the Capitanian ocean, respectively, which were constrained by the Akasaka $\delta^{15}N_{acid.}$ record and the local upwelling model (Figure 8). Their results are consistent with each other and strongly suggest that the Capitanian superocean was substantially reducing compared to the modern oceans.

5.4. Large $\delta^{15}N$ Oscillation in the Akasaka Limestone

In the middle to upper part of the present Akasaka limestone, the $\delta^{15}N_{acid.}$ values fluctuate largely with ∼8‰ amplitude (Figure 5). Although the depositional age of the analyzed limestone is not well-constrained due to the lack of conodont fossil, the fusuline biostratigraphy indicates that the analyzed ∼115-m-thick limestone accumulated in the early to latest Capitanian (Kofukuda et al., 2014; Ota & Isozaki, 2006; Zaw Win, 1999), possibly covering ∼4.8 Myr (Henderson et al., 2020). The 16–32 m periodicity therefore corresponds roughly to 670–1,300 kyr cyclicity, assuming that the accumulation rate was consistent through the analyzed succession. A ∼100-Myr-scale $\delta^{15}N$ fluctuations modulated by the long-term climate variation between icehouse-greenhouse modes was suggested through the Phanerozoic (Algeo et al., 2014), while shorter glacial-interglacial oscillation in $\delta^{15}N$ with 10 kyr periodicity was recorded in Quaternary marine sediments and planktonic foraminifera (e.g., Liu et al., 2008; Ren et al., 2017). The 670–1,300 kyr periodicity of $\delta^{15}N_{acid.}$ fluctuations with large amplitude (up to 8‰) recorded in the present Akasaka limestone is distinct from that of previously-known $\delta^{15}N$ oscillation in the Phanerozoic, suggesting the presence of unknown controlling factor on the Earth system with ∼1 Myr periodicity in its history.

As mentioned in Section 5.3.1, we constrained that the possible maximum ΔO_2 and minimum δ_D on which the Akasaka $\delta^{15}N_{acid.}$ range (+11‰ to +28‰) is fully covered within the range of R_U (0 cm/hr to 2.0 cm/hr) were

−80 μM and +9‰ (+2/–1‰), respectively, in the non-N-fixation case (Figure 8). The observed $\delta^{15}N_{acid.}$ fluctuations in the Akasaka limestone can be apparently explained by periodic changes in R_U between 0 cm/hr and 2 cm/hr, although it should be considered whether or not these supposed changes in R_U (similar to in the modern ODZs) were possible in the Capitanian Panthalassic Ocean. Previous model calculations suggested that, during the Permian–Triassic transition, the vertical velocity of a water mass in the surface ocean around the equator could be changed by > 1.6 cm/hr by precession-driven climate variability (Winguth & Winguth, 2013). Moreover, even in the annual cycle, the wind-induced vertical transport changes seasonally by ∼2.5 times (between ∼0.15 and ∼0.38 Sv) in the modern upwelling system off central-northern Chile (e.g., Bravo et al., 2016). Although large uncertainties (e.g., the paleo-latitude of the seamount during the deposition of the Akasaka limestone) still remain, those observations allow us to infer that the supposed changes in R_U (0 cm/hr to 2.0 cm/hr) for the Akasaka $\delta^{15}N_{acid.}$ record were possible in the Capitanian superocean.

In summary, we interpret that the long-term (∼1 Myr) $\delta^{15}N_{acid.}$ fluctuations of the Akasaka limestone were likely caused by the periodic changes in local upwelling rate of deep-water along the seamount at the top of which nitrogen fixation was permanently inhibited. The global redox structure of the superocean could have been rather stable during the Capitanian, the analyzed limestone accumulated, although our modeling results do not exclude the possibility of short-term (<670 kyr) change in ΔO_2 and δ_D (i.e., $\delta^{15}N_{NO3}$) in the Capitanian superocean. Such change in $\delta^{15}N_{NO3}$ might explain short-term $\delta^{15}N_{acid.}$ variation up to six‰ observed at the Akasaka and Chaotian sections (Saitoh et al., 2014).

The periodicity of the $\delta^{15}N_{acid.}$ fluctuations (ca. 670–1,300 kyr) (Figure 6) is apparently close to ∼1.2-Myr long obliquity cycle, originated from interaction between the orbital inclinations of Earth and Mars (the $s_3 - s_4$ term; Laskar et al., 2004). Although the $s_3 - s_4$ obliquity term could have been changed through geologic time due to the chaotic behavior of the Solar system (Laskar et al., 2004), its periodicity has been estimated to be ∼1 Myr in the Guadalupian (Fang et al., 2015, 2017). Thus, the Akasaka $\delta^{15}N_{acid.}$oscillation could have been paced with this astronomical cycle. The obliquity-paced latitudinal insolation difference and associated glacial dynamics and atmospheric circulation might have modulated the local upwelling rate of deep-water along the mid-Panthalassan seamount in the Capitanian.

5.5. Implications for the Global Extinction

The end-Guadalupian or "Capitanian" extinction was one of severe biodiversity crises in the Phanerozoic (Jin et al., 1994; Stanley & Yang, 1994), and several geological events in the Capitanian have been proposed as the cause of extinction, including the Emeishan volcanism in South China (Bond et al., 2020; Chung & Jahn, 1995; Grasby et al., 2016; Wignall et al., 2009; Zhou et al., 2002), a large regression (Jin et al., 1994), global warming and oceanic acidification (Clapham & Payne, 2011), severe cooling (Isozaki et al., 2007a, b), and marine anoxia/euxinia (Saitoh et al., 2013a). Although the Emeishan volcanism has been emphasized by many as the leading candidate for its trigger, the main kill mechanisms in marine and terrestrial realms are still controversial (e.g., Bond et al., 2020). One of the difficulties in constraining kill mechanisms for the "Capitanian" extinction is that the precise timing and pattern of the extinction remain unclear (Saitoh, 2021 and references therein). The extinction may have occurred gradually (Clapham et al., 2009; Yang et al., 2004) or stepwisely (Huang et al., 2019; Saitoh, 2021) in the Capitanian. On the other hand, Bond et al. (2010a, b) suggested that the major extinction occurred in the mid-Capitanian, significantly before the G–LB (cf., B. Zhang et al., 2019b).

In the Akasaka limestone, two extinction horizons are assigned in its uppermost ∼20-m-thick part (Figure 5 and Figure S1) (Kofukuda et al., 2014). As discussed in Section 5.3, the Akasaka $\delta^{15}N_{acid.}$ record suggests that the ODZs (with the sulfidic core) developed widely along the continental margins and were sustained in the substantially reducing ocean during the Capitanian (Figure 9), before the shelf extinction. Hence, the Akasaka limestone stratigraphy is apparently consistent with the scenario that the protracted development of anoxia/euxinia in the expanded ODZs along the continental margins served as a potential stress for shallow-marine biota during the Capitanian (Saitoh et al., 2014), although the timing and pattern of the global extinction should be better constrained by further studies.

6. Conclusions

A new nitrogen isotope ($\delta^{15}N$) record from a Capitanian (Late Guadalupian) mid-Panthalassic paleo-atoll limestone documents that the $\delta^{15}N$ values of limestones after acid treatment ($\delta^{15}N_{acid.}$) are substantially high up to

+28‰, the highest among all the previous marine records in the Phanerozoic. Assuming the upwelling system along the seamount, numerical modeling suggests that the $\delta^{15}N$ value of a global deep-oceanic nitrate reservoir was ≥+9‰ in the Capitanian, and that, at a regional scale, substantially ^{15}N-enriched nitrate was produced via denitrification in the subsurface ocean along the seamount and supplied to the surface water via upwelling. The $\delta^{15}N_{acid.}$ values fluctuate largely (<8‰ amplitude) and periodically (~670–1,300 kyr scale) in the analyzed succession, caused by periodic changes in upwelling rate of deep-water along the seamount in potential response to the previously-overlooked ~1 Myr astronomical cycle. Based on the isotopic and modeling results, we constrained the redox structure of the Capitanian Panthalassic Ocean on a global scale. The superocean may have been largely under dysoxic (~10 μM < the O_2 concentration < ~100 μM) conditions, and the waters at intermediate depths (100–1,000 m) (O_2 ≤ 20 μM on global average) were more reducing compared to the deeper/basal part of the oceans (O_2 ≤ 60 μM). In association with the substantial O_2 depletion at intermediate water depths, the oxygen-deficient zones (ODZ; O_2 < 5 μM) with the anoxic/euxinic core developed widely along the continental margins (≥~0.4% of global ocean volume; at least twice as much as in the modern oceans), persisting as a potential stress for shallow-marine biota during the stage. The present results highlight that a $\delta^{15}N$ record of a paleo-atoll limestone at the top of a mid-oceanic seamount is useful to constrain the vertical redox structure from a global perspective in the past ocean, in combination with global oceanographic modeling.

Appendix A: Explanatory Notes

Note 1: A term "oxygen minimum zone (OMZ)" has been commonly used for a water zone at an intermediate water depth (100–1,000 m) in the oceans where the O_2 concentration is at the lowest in the water column, although the OMZs may include water masses in which O_2 is still a major electron acceptor (Moffett, 2021). For example, Lam and Kuypers (2011) roughly defined the OMZ as a mid-depth water zone where the O_2 concentration is less than 20 μM. In order to focus on the nitrogen cycle in oxygen-depleted waters, we use the term "oxygen-deficient zone (ODZ)" in the present article as an oxygen-deficient water zone in which alternative electron acceptors (e.g., nitrate and sulfate) are predominantly used for respiration. In general, the ODZ is included within the OMZ according to its definition and corresponds to a mid-depth water zone where the O_2 concentration is less than 5 μM (Codispoti et al., 2005). On the environmental aqueous redox classification, the ODZ is included in the "suboxic zone" (O_2 < ~10 μM) of which upper limit is characterized by the NO_3^-/N_2 redox couple (Algeo & Li, 2020; Tyson and Pearson, 1991).

Note 2: The "nitrogenous" oceanic condition in the present upwelling model represents the oceanic condition in which fixed-N in the open-ocean boxes I and D is predominantly nitrate and denitrification occurs everywhere in these boxes. Under the "nitrogenous" oceanic condition, ODZs expand entirely to the boxes I and D.

Note 3: The relationships among the O_2 and NO_3^- concentrations in the box UM and the export production from box U to UM in the non-N-fixation case in the present local upwelling model (Figures 7a and 7b) are consistent with the spatial distribution of O_2 and NO_3^- in mid-depth waters within and along the modern Peruvian ODZ in the eastern tropical South Pacific (ETSP) (e.g., Peters et al., 2018). In the ETSP, the NO_3^- concentration of water masses within the ODZ core (O_2 < 1 μM) (corresponding to the high *EP* condition in the present upwelling model) is still ~20 μM. The NO_3^- concentration immediately below the Peruvian ODZ (O_2 ~ 30 μM) (corresponding to the low *EP* condition) is ~40 μM and higher than that in the deep ocean (~30 μM). The results of the present upwelling model are consistent with those observations of the modern ODZ.

Table A1
Parameters Used in the Five-Box Model

Parameters	Label	Value	Unit	Ref.
Vertical water exchange rate between U and UM	K_U	0.1	cm h^{-1}	Canfield (2006)
Vertical water exchange rate between UM and D	K_{UM}	0.1	cm h^{-1}	Canfield (2006)
Horizontal water exchange rate between UM and I	K_I	0.4	cm h^{-1}	Canfield (2006)
Advective upwelling from D to UM	A	0	cm h^{-1}	Canfield (2006)
Advective flow from I to UM	B	variable (0.4)	cm h^{-1}	Canfield (2006)
Remineralization ratio in the box UM	X	0.7	-	Canfield (2006)

Table A1
Continued

Parameters	Label	Value	Unit	Ref.
C/P ratio of POM	r_{CP}	117	mol mol^{-1}	Boyle et al. (2013)
N/P ratio of POM	r_{NP}	16	mol mol^{-1}	Canfield (2006)
N/C ratio of POM	r_{NC}	16/117	mol mol^{-1}	Boyle et al. (2013)
O_2:C_{org} ratio during aerobic respiration of POM	r_{O2C}	170/117	mol mol^{-1}	Boyle et al. (2013)
NO_3^- reduced/C_{org} oxidized ratio during denitrification	r_{deni}	0.8	mol mol^{-1}	Boyle et al. (2013)
SO_4^{2-} reduced/C_{org} oxidized ratio during microbial sulfate reduction	r_{MSR}	0.5	mol mol^{-1}	Boyle et al. (2013)
O_2 in box U	$O_{2,U}$	250	μM	Canfield (2006)
Deep water O_2 in the upwelling region	$O_{2,D}$	variable (140)	μM	Canfield (2006)
O_2 concentration in the I box	$O_{2,I}$	variable (100)	μM	Canfield (2006)
NO_3^- in box U	N_U	0	μM	Canfield (2006)
Deep water NO_3^- in the upwelling region	N_D	36.65	μM	Canfield (2006)
NO_3^- concentration in box I	N_I	40.43	μM	Canfield (2006)
NH_4^+ in box U	N^R_U	0	μM	Boyle et al. (2013)
Deep water NH_4^+ in the upwelling region	N^R_D	0	μM	Boyle et al. (2013)
NH_4^+ concentration in box I	N^R_I	0	μM	Boyle et al. (2013)
Deep water PO_4^{3-} in the upwelling region	P_D	2.29	μM	Canfield (2006)
PO_4^{3-} concentration in box I	P_I	2.53	μM	Canfield (2006)
$\delta^{15}N$ of the NO_3^- in box I	δ_I	variable (4.9), $\delta_D \pm 2$	‰	This study
$\delta^{15}N$ of the NO_3^- in box D	δ_D	variable (4.9)	‰	This study

Note. Values in parenthesis represents the reference value.

Table A2
Equations for Biogeochemical Fluxes (Non-N_2-Fixation Case)

Oxic upwelling zone ($O_{2,UM} > 0$)	Anoxic upwelling zone ($O_{2,UM} = 0$)
New production (EP)	
$EP = \frac{A+B+K_U}{r_{NC}}\left(N_{UM} + N^R_{UM}\right)$	$EP = \frac{A+B+K_U}{r_{NC}}\left(N_{UM} + N^R_{UM}\right)$
Aerobic respiration (R_{aero})	
$R_{aero} = xEP$	$R_{aero} = \frac{K_U O_{2,U} + (A+K_{UM})O_{2,D} + (K_I+B)O_{2,I}}{r_{O_2C}}$
Denitrification (R_{deni})	
$R_{deni} = 0$	$R_{deni} = xEP - R_{aero}$
Nitrate in the box UM (N_{UM})	
$N_{UM} = \frac{(A+K_{UM})N_D + (K_I+B)N_I + x(A+B+K_U)\frac{(A+K_{UM})N^R_D + (K_I+B)N^R_I}{A+B+K_U+K_{UM}+K_I}}{(1-x)(A+B+K_U)+K_{UM}+K_I}$	$N_{UM} = \frac{(A+K_{UM})N_D + (K_I+B)N_I + r_{NC}R_{aero} - r_{deni}R_{deni}}{A+B+K_U+K_{UM}+K_I}$
Ammonium in the box UM (N^R_{UM})	
$N^R_{UM} = \frac{(A+K_{UM})N^R_D + (B+K_I)N^R_I}{A+B+K_U+K_{UM}+K_I}$	$N^R_{UM} = \frac{(A+K_{UM})N^R_D + (B+K_I)N^R_I + r_{NC}R_{deni}}{A+B+K_U+K_{UM}+K_I}$
Dissolved O_2 in the box UM ($O_{2,UM}$)	
$O_{2,UM} = \frac{K_U O_{2,U} + (A+K_{UM})O_{2,D} + (K_I+B)O_{2,I} - r_{O_2C}xEP}{A+B+K_U+K_{UM}+K_I}$	$O_{2,UM} = 0$
$\delta^{15}N$ of N_{UM} (δ_{UM})	
$\delta_{UM} = \frac{\zeta + \eta\delta^R_{UM}N^R_{UM}}{1-\eta N_{UM}}\zeta = \frac{(A+K_{UM})\delta_D N_D + (K_I+B)\delta_I N_I}{(A+K_{UM})N_D + (K_I+B)N_I + r_{NC}R_{aero}}\eta = \frac{\frac{r_{NC}R_{aero}}{N_{UM}+N^R_{UM}}}{(A+K_{UM})N_D + (K_I+B)N_I + r_{NC}R_{aero}}$	$\delta_{UM} = \frac{\theta + \eta\delta^R_{UM}N^R_{UM}}{1-\eta N_{UM}}$ $\theta = \frac{(A+K_{UM})\delta_D N_D + (K_I+B)\delta_I N_I - r_{deni}\epsilon_{DW}R_{deni}}{(A+K_{UM})N_D + (K_I+B)N_I + r_{NC}R_{aero}}$

Table A2
Continued

Oxic upwelling zone ($O_{2,UM} > 0$)	Anoxic upwelling zone ($O_{2,UM} = 0$)
$\delta^{15}N$ of N^{R}_{UM} (δ^{R}_{UM})	
$\delta^{R}_{UM} = \frac{(A+K_{UM})\delta^{R}_{D}N^{R}_{D} + (K_I+B)\delta^{R}_{I}N^{R}_{I}}{(A+K_{UM})N^{R}_{D} + (K_I+B)N^{R}_{I}}$	$\delta^{R}_{UM} = \frac{\mu + \frac{\nu\theta}{1-\eta N_{UM}}}{1 - \frac{\nu\eta N^{R}_{UM}}{1-\eta N_{UM}}}$ $\mu = \frac{(A+K_{UM})\delta^{R}_{D}N^{R}_{D} + (K_I+B)\delta^{R}_{I}N^{R}_{I}}{(A+K_{UM})N^{R}_{D} + (K_I+B)N^{R}_{I} + \frac{N_{UM}}{N_{UM}+N^{R}_{UM}}r_{NC}(xEP - R_{aero})}$ $\nu = \frac{\frac{N_{UM}}{N_{UM}+N^{R}_{UM}}r_{NC}(xEP - R_{aero})}{(A+K_{UM})N^{R}_{D} + (K_I+B)N^{R}_{I} + \frac{N_{UM}}{N_{UM}+N^{R}_{UM}}r_{NC}(xEP - R_{aero})}$
$\delta^{15}N$ of PON (δ_{PON})	
$\delta_{PON} = \frac{\delta_{UM}N_{UM} + \delta^{R}_{UM}N^{R}_{UM}}{N_{UM}+N^{R}_{UM}}$	$\delta_{PON} = \frac{\delta_{UM}N_{UM} + \delta^{R}_{UM}N^{R}_{UM}}{N_{UM}+N^{R}_{UM}}$

Appendix B: Derivation of Equations in the Upwelling Model

We employ a five-box model of ocean biogeochemistry that was originally developed by Canfield (2006) and modified later by Boyle et al. (2013). The model consists of the surface ocean in the coastal upwelling region (U), the outer-ocean surface waters (S), the intermediate waters in the upwelling region (UM), the intermediate waters in the outer-ocean (I), and the deep waters (D) (see Figure 2 for the model schematic). A comprehensive explanation of the model design and empirical/theoretical basis are fully explained elsewhere (Boyle et al., 2013; Canfield, 2006). According to the model in Boyle et al. (2013), we explicitly include the fraction of POM remineralized in the box UM (x) and develop the mass balance calculation approach for assessing the nitrogen isotope value of fixed-N in our model.

We consider the series of mass balance equations in the upwelling region (box U and UM) and handle the other boxes for determining their boundary conditions. The central aim here is to provide the key equations and to highlight modifications from the former models (Boyle et al., 2013; Canfield, 2006). For the non-N_2-fixation case, the input pathway of nitrate and ammonium to box U is upwelling and vertical mixing. The derived fixed-N to box U is assimilated to the shallow-water biomass. A part of the particulate organic nitrogen (PON) is exported to the aphotic zone and this process represents the primary output of fixed-N from box U. The nitrogen mass balance equation is written as follows:

$$r_{NC}EP = (A + B + K_U)\left(N_{UM} + N^{R}_{UM}\right), \tag{A1}$$

where EP denotes the export production (in terms of organic carbon), and r_{NC} represents the N/C ratio of organic matter (=16/117). In this study, we calculate nitrogen isotope values of N and N^{R} considering its mass balance in box U and UM. Specifically, the isotopic mass balance in box U is written as follows:

$$\delta_{PON}r_{NC}EP = (A + B + K_U)\left(\delta_{UM}N_{UM} + \delta^{R}_{UM}N^{R}_{UM}\right), \tag{A2}$$

where δ_{PON} denotes the $\delta^{15}N$ value of PON, and δ_{UM} and δ^{R}_{UM} are the $\delta^{15}N$ value of N_{UM} and N^{R}_{UM}, respectively. The above equations are solved with respect to δ_{PON}:

$$\delta_{PON} = \frac{\delta_{UM}N_{UM} + \delta^{R}_{UM}N^{R}_{UM}}{N_{UM} + N^{R}_{UM}}. \tag{A3}$$

Therefore, the nitrogen isotope value of PON reflects the values of nitrate and ammonium in the box UM.

The mass balance equations for ammonium and its nitrogen isotope value in the box UM are written as follows:

$$(A + K_{UM})N^{R}_{D} + (B + K_I)N^{R}_{I} + r_{NC}(xEP - R_{aero}) = (A + B + K_U + K_{UM} + K_I)N^{R}_{UM}, \tag{A4}$$

$$(A + K_{UM})\delta^{R}_{D}N^{R}_{D} + (B + K_I)\delta^{R}_{I}N^{R}_{I} + r_{NC}\delta_{PON}(xEP - R_{aero}) = (A + B + K_U + K_{UM} + K_I)\delta^{R}_{UM}N^{R}_{UM}, \tag{A5}$$

where R_{aero} denotes the rate of aerobic respiration in the box UM (in terms of carbon). By using these equations, we have

$$(A + K_{UM})\left(\delta^{R}_{D} - \delta^{R}_{UM}\right)N^{R}_{D} + (B + K_{I})\left(\delta^{R}_{I} - \delta^{R}_{UM}\right)N^{R}_{I} + r_{NC}\left(\delta_{PON} - \delta^{R}_{UM}\right)(xEP - R_{aero}) = 0. \quad (A6)$$

When $O_{2UM} > 0$, POM is remineralized via aerobic respiration ($R_{aero} = xEP$). We can thus solve Equation (A6) with respect to δ^{R}_{UM}, as follows:

$$\delta^{R}_{UM} = \frac{(A + K_{UM})\delta^{R}_{D}N^{R}_{D} + (B + K_{I})\delta^{R}_{I}N^{R}_{I}}{(A + K_{UM})N^{R}_{D} + (B + K_{I})N^{R}_{I}}. \quad (A7)$$

Similarly, the mass balance equations for nitrate and its nitrogen isotope value in the box UM are written as follows:

$$(A + K_{UM})N_{D} + (B + K_{I})N_{I} + r_{NC}R_{aero} = (A + B + K_{U} + K_{UM} + K_{I})N_{UM}, \quad (A8)$$

$$(A + K_{UM})\delta_{D}N_{D} + (B + K_{I})\delta_{I}N_{I} + r_{NC}\delta_{PON}R_{aero} = (A + B + K_{U} + K_{UM} + K_{I})\delta_{UM}N_{UM}. \quad (A9)$$

By combining these equations, we can obtain

$$(A + K_{UM})(\delta_{D} - \delta_{UM})N_{D} + (B + K_{I})(\delta_{I} - \delta_{UM})N_{I} + r_{NC}(\delta_{PON} - \delta_{UM})R_{aero} = 0. \quad (A10)$$

For the oxic upwelling zone scenario ($O_{2UM} > 0$), we can solve Equation A10 with respect to δ_{UM} (see Table A2).

The mass balance equation for O_2 at the box UM is written as follows:

$$K_{U}O_{2_U} + (A + K_{UM})O_{2_d} + (B + K_{I})O_{2_i} = (A + B + K_{U} + K_{UM} + K_{I})O_{2_{UM}} + r_{O_2C}R_{aero}. \quad (A11)$$

Solving with respect to O_{2UM} yields

$$O_{2_{UM}} = \frac{K_{U}O_{2_U} + (A + K_{UM})O_{2_D} + (B + K_{I})O_{2_I} - r_{O_2C}R_{aero}}{A + B + K_{U} + K_{UM} + K_{I}}. \quad (A12)$$

For the anoxic upwelling zone ($O_{2UM} = 0$), the aerobic respiration flux can be obtained using Equation A12 with $O_{2UM} = 0$,

$$R_{aero} = \frac{K_{U}O_{2_U} + (A + K_{UM})O_{2_D} + (B + K_{I})O_{2_I}}{r_{O_2C}}. \quad (A13)$$

The mass balance equation of N_{UM} is modified by taking into account the denitrification,

$$(A + K_{UM})N_{D} + (B + K_{I})N_{I} + r_{NC}R_{aero} = (A + B + K_{U} + K_{UM} + K_{I})N_{UM} + r_{deni}R_{deni}, \quad (A14)$$

where r_{deni} (=0.8) denotes the stoichiometrical ratio between reduced nitrate and oxidized organic carbon via denitrification. The rate of denitrification is given as xEP-R_{aero} (for $N_{UM} > 0$). When Equation A14 yields a negative N_{UM} value, R_{deni} is obtained with Equation A14 by assuming $N_{UM} = 0$ and the remaining degradable organic matter (xEP-R_{aero}-R_{deni}) is assumed to be remineralized via sulfate reduction.

When the nitrogen fixation is not inhibited in box U, biological productivity is assumed to be limited by the availability of phosphorus:

$$EP = r_{CP}(A + B + K_{U})P_{UM}. \quad (A15)$$

The rate of nitrogen fixation is determined so that it can compensate the fixed-N demand for sustaining biological production:

$$F_{N_{fix}} = r_{NC}EP - (A + B + K_{U})\left(N_{UM} + N^{R}_{UM}\right). \quad (A16)$$

The isotopic mass balance equation for box U is written as follows:

$$(\delta_{atm} + \varepsilon_{fix})F_{N_{fix}} = \delta_{PON}r_{NC}EP - (A + B + K_{U})\left(\delta_{UM}N_{UM} + \delta^{R}_{UM}N^{R}_{UM}\right). \quad (A17)$$

By combining Equations A16 and A17, we can obtain

$$\delta_{\mathrm{PON}} = \frac{\delta_{\mathrm{UM}} N_{\mathrm{UM}} + \delta^{\mathrm{R}}_{\mathrm{UM}} N^{\mathrm{R}}_{\mathrm{UM}} + (\delta_{\mathrm{atm}} + \varepsilon_{\mathrm{fix}}) \frac{F_{\mathrm{Nfix}}}{A+B+K_{\mathrm{U}}}}{N_{\mathrm{UM}} + N^{\mathrm{R}}_{\mathrm{UM}} + \frac{F_{\mathrm{Nfix}}}{A+B+K_{\mathrm{U}}}}. \tag{A18}$$

The mass balance of phosphate in the box UM is

$$(A + K_{\mathrm{UM}})P_{\mathrm{D}} + (B + K_{\mathrm{I}})P_{\mathrm{I}} + \frac{xEP}{r_{\mathrm{CP}}} = (A + B + K_{\mathrm{U}} + K_{\mathrm{UM}} + K_{\mathrm{I}})P_{\mathrm{UM}}. \tag{A19}$$

Substituting Equation A15, we can obtain

$$P_{\mathrm{UM}} = \frac{(A + K_{\mathrm{UM}})P_{\mathrm{D}} + (B + K_{\mathrm{I}})P_{\mathrm{I}}}{A + B + K_{\mathrm{U}} + K_{\mathrm{UM}} + K_{\mathrm{I}} - x(A + B + K_{\mathrm{U}})}. \tag{A20}$$

Data Availability Statement

Data supporting this study are available at Saitoh (2023).

Acknowledgments
This study was supported by JSPS KAKENHI (JP16204040, JP20224012, JP26610159, JP15H03740, JP15H03741, JP17H06455). Kawai Lime and Mitsuboshi Mining allowed scientific drilling. Daisuke Kofukuda and Yohei Matsui assisted with sample selection and isotope analysis, respectively. Carlos Jaramillo and two anonymous reviewers gave us fruitful comments to improve the manuscript.

References

Akasaka Research Group. (1956). Geological study of the Akasaka limestone. *Chikyu Kagaku*, *26*(27), 10–18.

Algeo, T. J., & Li, C. (2020). Redox classification and calibration of redox thresholds in sedimentary systems. *Geochimica et Cosmochimica Acta*, *287*, 8–26. https://doi.org/10.1016/j.gca.2020.01.055

Algeo, T. J., Meyers, P. A., Robinson, R. S., Rowe, H., & Jiang, G. Q. (2014). Icehouse-greenhouse variations in marine denitrification. *Biogeosciences*, *11*(4), 1273–1295. https://doi.org/10.5194/bg-11-1273-2014

Altabet, M. A. (2001). Nitrogen isotopic evidence for micronutrient control of fractional NO_3^- utilization in the equatorial Pacific. *Limnology & Oceanography*, *46*(2), 368–380. https://doi.org/10.4319/lo.2001.46.2.0368

Altabet, M. A., & Francois, R. (1994). Sedimentary nitrogen isotopic ratio as a recorder for surface ocean nitrate utilization. *Global Biogeochemical Cycles*, *8*(1), 103–116. https://doi.org/10.1029/93GB03396

Awramik, S. M., & Buchheim, H. P. (2009). A giant, late Archean lake system: The Meentheena member (Tumbiana Formation; Fortescue Group), Western Australia. *Precambrian Research*, *174*(3–4), 215–240. https://doi.org/10.1016/j.precamres.2009.07.005

Berner, R. A. (2006). Geocarbsulf: A combined model for Phanerozoic atmospheric O_2 and CO_2. *Geochimica et Cosmochimica Acta*, *70*(23), 5653–5664. https://doi.org/10.1016/j.gca.2005.11.032

Bianchi, D., Dunne, J. P., Sarmiento, J. L., & Galbraith, E. D. (2012). Data-based estimates of suboxia, denitrification, and N_2O production in the ocean and their sensitivities to dissolved O_2. *Global Biogeochemical Cycles*, *26*(2), GB2009. https://doi.org/10.1029/2011GB004209

Bond, D. P. G., Hilton, J., Wignall, P. B., Ali, J. R., Stevens, L. G., Sun, Y. D., & Lai, X. L. (2010). The middle Permian (Capitanian) mass extinction on land and in the oceans. *Earth-Science Reviews*, *102*(1–2), 100–116. https://doi.org/10.1016/j.earscirev.2010.07.004

Bond, D. P. G., Wignall, P. B., Joachimski, M. M., Sun, Y. D., Savov, I., Grasby, S. E., et al. (2015). An abrupt extinction in the middle permian (capitanian) of the Boreal realm (Spitsbergen) and its link to anoxia and acidification. *GSA Bulletin*, *127*(9–10), 1411–1421. https://doi.org/10.1130/B31216.1

Bond, D. P. G., Wignall, P. B., Wang, W., Izon, G., Jiang, H. S., Lai, X. L., et al. (2010b). The mid-Capitanian (Middle Permian) mass extinction and carbon isotope record of South China. *Palaeogeography, Palaeoclimatology, Palaeoecology*, *292*(1–2), 282–294. https://doi.org/10.1016/j.palaeo.2010.03.056

Bond, D. P. G., Wignall, P. B., & Grasby, S. E. (2020). The capitanian (Guadalupian, middle Permian) mass extinction in NW Pangea (Borup Fiord, Arctic Canada): A global crisis driven by volcanism and anoxia. *GSA Bulletin*, *132*(5–6), 931–942. https://doi.org/10.1130/B35281.1

Böning, P., Brumsack, H.-J., Böttcher, M. E., Schnetger, B., Kriete, C., Kallmeyer, J., & Borchers, S. L. (2004). Geochemistry of Peruvian near-surface sediments. *Geochimica et Cosmochimica Acta*, *68*(21), 4429–4451. https://doi.org/10.1016/j.gca.2004.04.027

Borchers, S. L., Schnetger, B., Böning, P., & Brumsack, H.-J. (2005). Geochemical signatures of the Namibian diatom belt: Perennial upwelling and intermittent anoxia. *Geochemistry, Geophysics, Geosystems*, *6*, Q06006. https://doi.org/10.1029/2004GC000886

Boyle, R. A., Clark, J. R., Poulton, S. W., Shields-Zhou, G., Canfield, D. E., & Lenton, T. M. (2013). Nitrogen cycle feedbacks as a control on euxinia in the mid-Proterozoic ocean. *Nature Communications*, *4*(1), 1533. https://doi.org/10.1038/ncomms2511

Brandes, J. A., & Devol, A. H. (2002). A global marine-fixed nitrogen isotopic budget: Implications for Holocene nitrogen cycling. *Global Biogeochemical Cycles*, *16*(4), 1120–1121. https://doi.org/10.1029/2001GB001856

Bravo, L., Ramos, M., Astudillo, O., Dewitte, B., & Goubanova, K. (2016). Seasonal variability of the Ekman transport and pumping in the upwelling system off central-northern Chile (~30°S) based on a high-resolution atmospheric regional model (WRF). *Ocean Science*, *12*(5), 1049–1065. https://doi.org/10.5194/os-12-1049-2016

Bristow, T. F., Kennedy, M. J., Derkowski, A., Droser, M. L., Jiang, G. Q., & Creaser, R. A. (2009). Mineralogical constraints on the paleoenvironments of the Ediacaran Doushantuo formation. *Proceedings of the National Academy of Sciences*, *106*(32), 13190–13195. https://doi.org/10.1073/pnas.0901080106

Brodie, C. R., Heaton, T. H. E., Leng, M. J., Kendrick, C. P., Casford, J. S. L., & Lloyd, J. M. (2011). Evidence for bias in measured $\delta^{15}N$ values of terrestrial and aquatic organic materials due to pre-analysis acid treatment methods. *Rapid Communications in Mass Spectrometry*, *25*(8), 1089–1099. https://doi.org/10.1002/rcm.4970

Buick, R. (1992). The antiquity of oxygenic photosynthesis: Evidence from stromatolites in sulphate-deficient Archaean lakes. *Science*, *155*(5040), 74–77. https://doi.org/10.1126/science.11536492

Canfield, D. E. (2006). Models of oxic respiration, denitrification and sulfate reduction in zones of coastal upwelling. *Geochimica et Cosmochimica Acta*, *70*(23), 5753–5765. https://doi.org/10.1016/j.gca.2006.07.023

Chung, S. L., & Jahn, B. M. (1995). Plume-lithosphere interaction in generation of the Emeishan flood basalts at the Permian-Triassic boundary. *Geology*, *23*, 889–892. https://doi.org/10.1130/0091-7613(1995)023<0889:pliigo>2.3.co;2

Clapham, M. E., & Payne, J. L. (2011). Acidification, anoxia, and extinction: A multiple logistic regression analysis of extinction selectivity during the middle and late permian. *Geology*, *39*(11), 1059–1062. https://doi.org/10.1130/G32230.1

Clapham, M. E., Shen, S. Z., & Bottjer, D. J. (2009). The double mass extinction revisited: Reassessing the severity, selectivity, and causes of the end-Guadalupian biotic crisis (late permian). *Paleobiology*, *35*(1), 32–50. https://doi.org/10.1666/08033.1

Codispoti, L. A., Yoshinari, T., & Devol, A. H. (2005). Suboxic respiration in the oceanic water column. In P. del Giorgio & P. Williams (Eds.), *Respiration in aquatic ecosystems* (pp. 225–247). Oxford University Press. https://doi.org/10.1093/acprof:oso/9780198527084.003.0012

Dalsgaard, T., Stewart, F. J., Thamdrup, B., Brabandere, L. D., Revsbech, N. P., Ulloa, O., et al. (2014). Oxygen at nanomolar levels reversibly suppresses process rates and gene expression in anammox and denitrification in the oxygen minimum zone off Northern Chile. *mBio*, *5*(6), e20. https://doi.org/10.1128/mBio.01966-14

Elrick, M., Polyak, V., Algeo, T. J., Romaniello, S., Asmerom, Y., Herrmann, A. D., et al. (2017). Global-ocean redox variation during the middle-late Permian through Early Triassic based on uranium isotope and Th/U trends of marine carbonates. *Geology*, *45*(2), 163–166. https://doi.org/10.1130/G38585.1

Falkowski, P. G. (1997). Evolution of the nitrogen cycle and its influence on the biological sequestration of CO_2 in the ocean. *Nature*, *387*(6630), 272–275. https://doi.org/10.1038/387272a0

Fang, Q., Wu, H. C., Hinnov, L. A., Jing, X. C., Wang, X. L., & Jiang, Q. C. (2015). Geologic evidence for chaotic behavior of the planets and its constraints on the third-order eustatic sequences at the end of the Late Paleozoic Ice Age. *Palaeogeography, Palaeoclimatology, Palaeoecology*, *440*, 848–859. https://doi.org/10.1016/j.palaeo.2015.10.014

Fang, Q., Wu, H. C., Hinnov, L. A., Jing, X. C., Wang, X. L., Yang, T. S., et al. (2017). Astronomical cycles of middle Permian Maokou formation in South China and their implications for sequence stratigraphy and paleoclimate. *Palaeogeography, Palaeoclimatology, Palaeoecology*, *474*, 130–139. https://doi.org/10.1016/j.palaeo.2016.07.037

Forryan, A., Naveira Garabato, A. C. N., Vic, C., Nurser, A. J. G., & Hearn, A. R. (2021). Galápagos upwelling driven by localized wind–front interactions. *Scientific Reports*, *11*(1), 1277. https://doi.org/10.1038/s41598-020-80609-2

Fripiat, F., Marconi, D., Rafter, P. A., Sigman, D. M., Altabet, M. A., Bourbonnais, A., et al. (2021). Compilation of nitrate $\delta^{15}N$ in the ocean. *PANGAEA*. https://doi.org/10.1594/PANGAEA.936484

Froelich, P. N., Klinkhammer, G. P., Bender, M. L., Luedtke, N. A., Heath, G. R., Cullen, D., et al. (1979). Early oxidation of organic matter in pelagic sediments of the eastern equatorial Atlantic: Suboxic diagenesis. *Geochimica et Cosmochimica Acta*, *43*(7), 1075–1090. https://doi.org/10.1016/0016-7037(79)90095-4

Fujisaki, W., Matsui, Y., Ueda, H., Sawaki, Y., Suzuki, K., & Maruoka, T. (2021). Pre-treatment methods for accurate determination of total nitrogen and organic carbon contents and their stable isotopic compositions: Re-evaluation from geological reference materials. *Geostandards and Geoanalytical Research*, *46*(1), 5–19. https://doi.org/10.1111/ggr.12410

Fujisaki, W., Sawaki, Y., Matsui, Y., Yamamoto, S., Isozaki, Y., & Maruyama, S. (2019). Redox condition and nitrogen cycle in the permian deep mid-ocean: A possible contrast between Panthalassa and Tethys. *Global and Planetary Change*, *172*, 179–199. https://doi.org/10.1016/j.gloplacha.2018.09.015

Galloway, J. N. (2014). The global nitrogen cycle. In K. K. Turekian & H. D. Holland (Eds.), *Treatise on geochemistry* (2nd ed., pp. 475–498). Elsevier. https://doi.org/10.1016/B978-0-08-095975-7.00812-3

Grasby, S. E., Beauchamp, B., Bond, D. P. G., Wignall, P. B., & Sanei, H. (2016). Mercury anomalies associated with three extinction events (capitanian crisis, latest Permian extinction and the Smithian/Spathian extinction) in NW Pangea. *Geological Magazine*, *153*(2), 285–297. https://doi.org/10.1017/S0016756815000436

Henderson, C. M., Shen, S. Z., Gradstein, F. M., & Agterberg, F. P. (2020). The permian period. *Geologic Time Scale*, *2*, 875–902. https://doi.org/10.1016/B978-0-12-824360-2.00024-3

Huang, Y. G., Chen, Z. Q., Wignall, P. B., Grasby, S. E., Zhao, L. S., Wang, X. D., & Kaiho, K. (2019). Biotic responses to volatile volcanism and environmental stresses over the Guadalupian-Lopingian (Permian) transition. *Geology*, *47*, 175–178. https://doi.org/10.1130/G45283.1

Isozaki, Y. (1997). Permo-Triassic boundary superanoxia and stratified superocean: Records from lost deep-sea. *Science*, *276*(5310), 235–238. https://doi.org/10.1126/science.276.5310.235

Isozaki, Y. (2009). Integrated "plume winter" scenario for the double-phased extinction during the Paleozoic-Mesozoic transition: The G-LB and P-TB events from a Panthalassan perspective. *Journal of Asian Earth Sciences*, *36*(6), 459–480. https://doi.org/10.1016/j.jseaes.2009.05.006

Isozaki, Y. (2014). Memories of pre-Jurassic lost oceans: How to retrieve them from extant lands. *Geoscience Canada*, *41*(3), 283–311. https://doi.org/10.12789/geocanj.2014.41.050

Isozaki, Y., Aljinovic, D., & Kawahata, H. (2011). The Guadalupian (permian) Kamura event in European Tethys. *Palaeogeography, Palaeoclimatology, Palaeoecology*, *308*(1–2), 12–21. https://doi.org/10.1016/j.palaeo.2010.09.034

Isozaki, Y., Kawahata, H., & Minoshima, K. (2007b). The Capitanian (Permian) Kamura cooling event: The beginning of the Paleozoic-Mesozoic transition. *Palaeoworld*, *16*(1–3), 16–30. https://doi.org/10.1016/j.palwor.2007.05.011

Isozaki, Y., Kawahata, H., & Ota, A. (2007a). A unique carbon isotope record across the Guadalupian-Lopingian (Middle-Upper Permian) boundary in mid-oceanic paleo-atoll carbonates: The high-productivity "Kamura event" and its collapse in Panthalassa. *Global and Planetary Change*, *55*(1–3), 21–38. https://doi.org/10.1016/j.gloplacha.2006.06.006

Isozaki, Y., Maruyama, S., & Furuoka, F. (1990). Accreted oceanic materials in Japan. *Techtonophysics*, *181*(1–4), 179–205. https://doi.org/10.1016/0040-1951(90)90016-2

Isozaki, Y., & Ota, A. (2001). Middle-upper Permian (Maokouan–Wuchiapingian) boundary in mid-oceanic paleo-atoll limestone of Kamura and Akasaka, Japan. *Proceedings of the Japan Academy, Series B*, *77*(6), 104–109. https://doi.org/10.2183/pjab.77.104

Jia, Y., & Kerrich, R. (2004). Nitrogen 15-enriched Precambrian kerogen and hydrothermal systems. *Geochemistry, Geophysics, Geosystems*, *5*(7), Q07005. https://doi.org/10.1029/2004GC000716

Jin, Y. G., Zhang, J., & Shang, Q. H. (1994). Two phases of the end-Permian mass extinction. In A. F. Embry, B. Beauchamp, & D. J. Glass (Eds.), *Pangea: Global environments and resources* (Vol. 17, pp. 813–822). Canadian Society of Petroleum Geologists.

Johnson, K. S., Berelson, W. M., Coale, K. H., Coley, T. L., Elrod, V. A., Fairey, W. R., et al. (1992). Manganese flux from continental margin sediments in a transect through the oxygen minimum. *Science*, *257*(5074), 1242–1245. https://doi.org/10.1126/science.257.5074.1242

Kakuwa, Y. (2008). Evaluation of palaeo-oxygenation of the ocean bottom across the Permian–Triassic boundary. *Global and Planetary Change*, *63*(1), 40–56. https://doi.org/10.1016/j.gloplacha.2008.05.002

Kametaka, M., Takebe, M., Nagai, H., Zhu, S., & Takayanagi, Y. (2005). Sedimentary environments of the middle permian phosphorite–chert complex from the northeastern Yangtze platform, China; the Gufeng formation: A continental shelf radiolarian chert. *Sedimentary Geology*, *174*(3–4), 197–222. https://doi.org/10.1016/j.sedgeo.2004.12.005

Kani, T., Hisanabe, C., & Isozaki, Y. (2013). The Capitanian (Permian) minimum of $^{87}Sr/^{86}Sr$ ratio in the mid-Panthalassan paleo-atoll carbonates and its demise by the deglaciation and continental doming. *Gondwana Research*, *24*(1), 212–221. https://doi.org/10.1016/j.gr.2012.08.025

Kanmera, K., & Nishi, H. (1983). Accreted oceanic reef complex in Southwest Japan. In M. Hashimoto & S. Uyeda (Eds.), *Accretion tectonics in the Circum-Pacific regions* (pp. 195–206). Terra Scientific Publishing. https://doi.org/10.1007/978-94-009-7102-8_14

Kast, E. R., Stolper, D. A., Auderset, A., Higgins, J. A., Ren, H., Wang, X. T., et al. (2019). Nitrogen isotope evidence for expanded ocean suboxia in the early Cenozoic. *Science*, *364*(6438), 386–389. https://doi.org/10.1126/science.aau5784

Kato, Y., Nakao, K., & Isozaki, Y. (2002). Geochemistry of late Permian to early Triassic pelagic cherts from southwest Japan: Implications for an oceanic redox change. *Chemical Geology*, *182*(1), 15–34. https://doi.org/10.1016/S0009-2541(01)00273-X

Kidder, D. L., & Worsley, T. R. (2010). Phanerozoic large igneous provinces (LIPs), HEATT (haline euxinic acidic thermal transgression) episodes, and mass extinctions. *Palaeogeography, Palaeoclimatology, Palaeoecology*, *295*(1–2), 162–191. https://doi.org/10.1016/j.palaeo.2010.05.036

Kobayashi, F. (2011). Permian fusuline faunas and biostratigraphy of the Akasaka Limestone (Japan). *Revue de Paléobiologie*, *30*, 431–574.

Kofukuda, D., Isozaki, Y., & Igo, H. (2014). A remarkable sea-level drop and relevant biotic responses across the Guadalupian–Lopingian (Permian) boundary in low-latitude mid-Panthalassa: Irreversible changes recorded in accreted paleo-atoll limestones in Akasaka and Ishiyama, Japan. *Journal of Asian Earth Sciences*, *82*, 47–65. https://doi.org/10.1016/j.jseaes.2013.12.010

Lam, P., & Kuypers, M. M. M. (2011). Microbial nitrogen cycling processes in oxygen minimum zones. *Annual Review of Marine Science*, *3*(1), 317–345. https://doi.org/10.1146/annurev-marine-120709-142814

Laskar, J., Robutel, P., Joutel, F., Gastineau, M., Correia, A. C. M., & Levrard, B. (2004). A long-term numerical solution for the insolation quantities of the Earth. *Astronomy and Astrophysics*, *428*(1), 261–285. https://doi.org/10.1051/0004-6361:20041335

Lavik, G., Stührmann, T., Brüchert, V., Van der Plas, A., Mohrholz, V., Lam, P., et al. (2009). Detoxification of sulphidic African shelf waters by blooming chemolithotrophs. *Nature*, *457*(7229), 581–584. https://doi.org/10.1038/nature07588

Liu, Z. H., Altabet, M. A., & Herbert, T. D. (2008). Plio-pleistocene denitrification in the eastern tropical North Pacific: Intensification at 2.1 Ma. *Geochemistry, Geophysics, Geosystems*, *9*(11), Q11006. https://doi.org/10.1029/2008GC002044

Martínez-García, A., Jung, J., Ai, X. E., Sigman, D. M., Auderset, A., Duprey, N. N., et al. (2022). Laboratory assessment of the impact of chemical oxidation, mineral dissolution, and heating on the nitrogen isotopic composition of fossil-bound organic matter. *Geochemistry, Geophysics, Geosystems*, *23*(8), e2022GC010396. https://doi.org/10.1029/2022GC010396

Matsuda, T., & Isozaki, Y. (1991). Well-documented travel history of Mesozoic pelagic chert in Japan: From remote ocean to subduction zone. *Tectonics*, *10*(2), 475–499. https://doi.org/10.1029/90TC02134

Matsuo, M., Kubo, K., & Isozaki, Y. (2003). Mössbauer spectroscopic study on characterization of iron in the Permian to Triassic deep-sea chert from Japan. *Hyperfine Interactions*, *5*, 435–438. https://doi.org/10.1007/978-94-010-0281-3_107

McManus, J., Berelson, W. M., Severmann, S., Johnson, K. S., Hammond, D. E., Roy, M., & Coale, K. H. (2012). Benthic manganese fluxes along the Oregon–California continental shelf and slope. *Continental Shelf Research*, *43*, 71–85. https://doi.org/10.1016/j.csr.2012.04.016

Meyers, P. A. (1994). Preservation of elemental and isotopic source identification of sedimentary organic matter. *Chemical Geology*, *114*(3–4), 289–302. https://doi.org/10.1016/0009-2541(94)90059-0

Moffett, J. W. (2021). Iron(II) in the world's oxygen deficient zones. *Chemical Geology*, *580*, 120314. https://doi.org/10.1016/j.chemgeo.2021.120314

Morford, J. L., & Emerson, S. (1999). The geochemistry of redox sensitive trace metals in sediments. *Geochimica et Cosmochimica Acta*, *63*(11–12), 1735–1750. https://doi.org/10.1016/S0016-7037(99)00126-X

Muttoni, G., Gaetani, M., Kent, D. V., Sciunnach, D., Angiolini, L., Berra, F., et al. (2009). Opening of the Neo-Tethys Ocean and the Pangea B to Pangea A transformation during the Permian. *GeoArabia*, *14*(4), 17–48. https://doi.org/10.2113/geoarabia140417

Nameroff, T. J., Balistrieri, L. S., & Murray, J. W. (2002). Suboxic trace metal geochemistry in the eastern tropical North Pacific. *Geochimica et Cosmochimica Acta*, *66*(7), 1139–1158. https://doi.org/10.1016/S0016-7037(01)00843-2

Nishizawa, M., Miyazaki, J., Makabe, A., Koba, K., & Takai, K. (2014). Physiological and isotopic characteristics of nitrogen fixation by hyperthermophilic methanogens: Key insights into nitrogen anabolism of the microbial communities in Archean hydrothermal systems. *Geochimica et Cosmochimica Acta*, *138*, 117–135. https://doi.org/10.1016/j.gca.2014.04.021

Nishizawa, M., Sano, Y., Ueno, Y., & Maruyama, S. (2007). Speciation and isotope ratios of nitrogen in fluid inclusions from seafloor hydrothermal deposits at 3.5 Ga. *Earth and Planetary Science Letters*, *254*(3–4), 332–344. https://doi.org/10.1016/j.epsl.2006.11.044

Nishizawa, M., Yamamoto, H., Ueno, Y., Tsuruoka, S., Shibuya, T., Sawaki, Y., et al. (2010). Grain-scale iron isotopic distribution of pyrite from Precambrian shallow marine carbonate revealed by a femtosecond laser ablation multicollector ICP-MS technique: Possible proxy for the redox state of ancient seawater. *Geochimica et Cosmochimica Acta*, *74*(9), 2760–2778. https://doi.org/10.1016/j.gca.2010.02.014

Onoue, T., Soda, K., & Isozaki, Y. (2021). Development of deep-sea anoxia in Panthalassa during the Lopingian (Late Permian): Insights from redox-sensitive elements and multivariate analysis. *Frontiers of Earth Science*, *8*, 613126. https://doi.org/10.3389/feart.2020.613126

Ota, A., & Isozaki, Y. (2006). Fusuline biotic turnover across the Guadalupian–Lopingian (Middle–Upper Permian) boundary in mid-oceanic carbonate buildups: Biostratigraphy of accreted limestone in Japan. *Journal of Asian Earth Sciences*, *26*(3–4), 353–368. https://doi.org/10.1016/j.jseaes.2005.04.001

Ozaki, K., & Tajika, E. (2013). Biogeochemical effects of atmospheric oxygen concentration, phosphorus weathering, and sea-level stand on oceanic redox chemistry: Implications for greenhouse climates. *Earth and Planetary Science Letters*, *373*, 129–139. https://doi.org/10.1016/j.epsl.2013.04.029

Ozawa, T., & Nishiwaki, N. (1992). *Permian Tethyan biota and sedimentary facies of the Akasaka limestone Group. Guidebook for 29th IGP field trip B13* (pp. 189–195). Nagoya University.

Papineau, D., Purohit, R., Goldberg, T., Pi, D., Shields, G. A., Bhu, H., et al. (2009). High primary productivity and nitrogen cycling after the Paleoproterozoic phosphogenic event in the Aravalli Supergroup, India. *Precambrian Research*, *171*(1–4), 37–56. https://doi.org/10.1016/j.precamres.2009.03.005

Peters, B. D., Lam, P. J., & Casciotti, K. L. (2018). Nitrogen and oxygen isotope measurements of nitrate along the US GEOTRACES Eastern Pacific Zonal Transect (GP16) yield insights into nitrate supply, remineralization, and water mass transport. *Marine Chemistry*, *201*, 137–150. https://doi.org/10.1016/j.marchem.2017.09.009

Peters, K. E., Sweeney, R. E., & Kaplan, I. R. (1978). Correlation of carbon and nitrogen stable isotope ratios in sedimentary organic matter. *Limnology & Oceanography*, *23*(4), 598–604. https://doi.org/10.4319/lo.1978.23.4.0598

Ren, H. J., Sigman, D. M., Martinez-Garcia, A., Anderson, R. F., Chen, M.-T., Ravelo, A. C., et al. (2017). Impact of glacial/interglacial sea level change on the ocean nitrogen cycle. *Proceedings of the National Academy of Sciences*, *114*(33), E6759–E6766. https://doi.org/10.1073/pnas.1701315114

Robinson, R. S., Kienast, M., Albuquerque, A. L., Altabet, M., Contreras, S., Holz, R. D. P., et al. (2012). A review of nitrogen isotopic alteration in marine sediments. *Paleoceanography*, *27*, PA4203. https://doi.org/10.1029/2012PA002321

Roy, A. B., & Paliwal, B. S. (1981). Evolution of lower proterozoic epicontinental deposits: Stromatolite-bearing Aravalli rocks of Udaipur, Rajasthan, India. *Precambrian Research*, *14*(1), 49–74. https://doi.org/10.1016/0301-9268(81)90035-8

Saitoh, M. (2021). Multiple sulfur isotope geochemistry during the Permian-Triassic transition. *Geosciences*, *11*(8), 327. https://doi.org/10.3390/geosciences110803277

Saitoh, M. (2023). Nitrogen isotope record from a mid-oceanic paleo-atoll limestone to constrain the redox state of the Panthalassa Ocean in the Capitanian (Late Guadalupian, Permian). [Dataset]. Zenodo. https://doi.org/10.5281/zenodo.7796655

Saitoh, M., Isozaki, Y., Ueno, Y., Yoshida, N., Yao, J. X., & Ji, Z. S. (2013b). Middle-Upper Permian carbon isotope stratigraphy at Chaotian, South China: Pre-extinction multiple upwelling of oxygen-depleted water onto continental shelf. *Journal of Asian Earth Sciences*, *67*(68), 51–62. https://doi.org/10.1016/j.jseaes.2013.02.009

Saitoh, M., Isozaki, Y., Yao, J. X., Ji, Z. S., Ueno, Y., & Yoshida, N. (2013a). The appearance of an oxygen-depleted condition on the Capitanian disphotic slope/basin in South China: Middle-Upper Permian stratigraphy at Chaotian in northern Sichuan. *Global and Planetary Change*, *105*, 180–192. https://doi.org/10.1016/j.gloplacha.2012.01.002

Saitoh, M., Ueno, Y., Isozaki, Y., Nishizawa, M., Shozugawa, K., Kawamura, T., et al. (2014). Isotopic evidence for water-column denitrification and sulfate reduction at the end-Guadalupian (Middle Permian). *Global and Planetary Change*, *123*, 110–120. https://doi.org/10.1016/j.gloplacha.2014.10.014

Saitoh, M., Ueno, Y., Matsu'ura, F., Kawamura, T., Isozaki, Y., Yao, J. X., et al. (2017). Multiple sulfur isotope records at the end-Guadalupian (Permian) at Chaotian, China: Implications for a role of bioturbation in the Phanerozoic sulfur cycle. *Journal of Asian Earth Sciences*, *135*, 70–79. https://doi.org/10.1016/j.jseaes.2016.12.009

Sakagami, S. (1980). Preliminary note on the upper part of the Akasaka limestone Group, Japan. *Proceedings of the Japan Academy, Series B*, *56*(1), 25–29. https://doi.org/10.2183/pjab.56.25

Sakurai, R., Ito, M., Ueno, Y., Kitajima, K., & Maruyama, S. (2005). Facies architecture and sequence-stratigraphic features of the Tumbiana Formation in the Pilbara Craton, northwestern Australia: Implications for depositional environments of oxygenic stromatolites during the Late Archean. *Precambrian Research*, *138*(3–4), 255–273. https://doi.org/10.1016/j.precamres.2005.05.008

Sano, H. (1988). Permian oceanic-rocks of Mino Terrane, central Japan Part II. Limestone facies. *The Journal of the Geological Society of Japan*, *94*(12), 963–976. https://doi.org/10.5575/geosoc.94.963

Sano, Y., & Pillinger, C. T. (1990). Nitrogen isotopes and N_2/Ar ratios in cherts: An attempt to measure time evolution of atmospheric $\delta^{15}N$ value. *Geochemical Journal*, *24*(5), 315–325. https://doi.org/10.2343/geochemj.24.315

Schlacher, T. A., & Connolly, R. M. (2014). Effects of acid treatment on carbon and nitrogen stable isotope ratios in ecological samples: A review and synthesis. *Methods in Ecology and Evolution*, *5*(6), 541–550. https://doi.org/10.1111/2041-210X.12183

Schoepfer, S. D., Henderson, C. M., Garrison, G. H., & Ward, P. D. (2012). Cessation of a productive coastal upwelling system in the Panthalassic Ocean at the Permian-Triassic boundary. *Palaeogeography, Palaeoclimatology, Palaeoecology*, *313–314*, 181–188. https://doi.org/10.1016/j.palaeo.2011.10.019

Schunck, H., Lavik, G., Desai, D. K., Großkopf, T., Kalvelage, T., Löscher, C. R., et al. (2013). Giant hydrogen sulfide plume in the oxygen minimum zone off Peru supports chemolithoautotrophy. *PLoS One*, *8*, e68661. https://doi.org/10.1371/journal.pone.0068661

Shi, L., Feng, Q., Shen, J., Ito, T., & Chen, Z. Q. (2016). Proliferation of shallow-water radiolarians coinciding with enhanced oceanic productivity in reducing conditions during the middle Permian, South China: Evidence from the Gufeng formation of Western Hubei province. *Palaeogeography, Palaeoclimatology, Palaeoecology*, *444*, 1–14. https://doi.org/10.1016/j.palaeo.2015.11.031

Sigman, D. M., & Fripiat, F. (2019). Nitrogen isotopes in the ocean. In J. K. Cochran, H. Bokuniewicz, & P. Yager (Eds.), *Encyclopedia of ocean sciences* (3rd ed., pp. 263–278). Academic. https://doi.org/10.1016/B978-0-12-409548-9.11605-7

Stanley, S. M., & Yang, X. (1994). A double mass extinction at the end of the Paleozoic era. *Science*, *266*(5189), 1340–1344. https://doi.org/10.1126/science.266.5189.1340

Stüeken, E. E., Buick, R., & Schauer, A. J. (2015). Nitrogen isotope evidence for alkaline lakes on late Archean continents. *Earth and Planetary Science Letters*, *411*, 1–10. https://doi.org/10.1016/j.epsl.2014.11.037

Thomazo, C., Ader, M., & Philippot, P. (2011). Extreme ^{15}N-enrichments in 2.72-Gyr-old sediments: Evidence for a turning point in the nitrogen cycle. *Geobiology*, *9*(2), 107–120. https://doi.org/10.1111/j.1472-4669.2011.00271.x

Thorne, A. M., & Trendall, A. F. (2001). Geology of the Fortescue Group, Pilbara Craton, Western Australia. *Western Australia Geological Survey, Bulletin*, *144*, 1–249.

Torrence, C., & Compo, G. P. (1998). A practical guide to wavelet analysis. *Bulletin of the American Meteorological Society*, *79*, 61–78. https://doi.org/10.1175/1520-0477(1998)079<0061:apgtwa>2.0.co;2

Tribovillard, N., Algeo, T. J., Lyons, T., & Riboulleau, A. (2006). Trace metals as paleoredox and paleoproductivity proxies: An update. *Chemical Geology*, *232*(1–2), 12–32. https://doi.org/10.1016/j.chemgeo.2006.02.012

Tyson, R. V., & Pearson, T. H. (1991). Modern and ancient continental shelf anoxia: An overview. In R. V. Tyson & T. H. Pearson (Eds.), *Modern and ancient continental shelf anoxia* (Vol. 58, pp. 1–24). Geological Society. https://doi.org/10.1144/GSL.SP.1991.058.01.01.Sp

Wada, E. (1980). Nitrogen isotope fractionation and its significance in biogeochemical processes occurring in marine environment s. In E. D. Goldberg, Y. Horibe, & K. Saruhashi (Eds.), *Isotope marine chemistry* (pp. 375–398). Uchida Rokakuho Pub. Co. Ltd.

Wang, X. Q., Jiang, G. Q., Shi, X. Y., Peng, Y. B., & Morales, D. C. (2018). Nitrogen isotope constraints on the early Ediacaran ocean redox structure. *Geochimica et Cosmochimica Acta*, *240*, 220–235. https://doi.org/10.1016/j.gca.2018.08.034

Wei, H. Y., Tang, Z. W., Yan, D., Wang, J. G., & Roberts, A. P. (2019). Guadalupian (Middle Permian) ocean redox evolution in South China and its implications for mass extinction. *Chemical Geology*, *530*, 119318. https://doi.org/10.1016/j.chemgeo.2019.119318

Wei, H. Y., Wei, X. M., Qiu, Z., Song, H. Y., & Shi, G. (2016). Redox conditions across the G–L boundary in South China: Evidence from pyrite morphology and sulfur isotopic compositions. *Chemical Geology*, *440*, 1–14. https://doi.org/10.1016/j.chemgeo.2016.07.009

Wignall, P. B., Sun, Y. D., Bond, D. P. G., Izon, G., Newton, R. J., Védrine, S., et al. (2009). Volcanism, mass extinction, and carbon isotope fluctuations in the Middle Permian of China. *Science*, *324*(5931), 1179–1182. https://doi.org/10.1126/science.1171956

Winguth, A., & Winguth, C. (2013). Precession-driven monsoon variability at the Permian–Triassic boundary – Implications for anoxia and the mass extinction. *Global and Planetary Change*, *105*, 160–170. https://doi.org/10.1016/j.gloplacha.2012.06.006

Yan, D., Liqin, Z., & Zhen, Q. (2013). Carbon and sulfur isotopic fluctuations associated with the end-Guadalupian mass extinction in South China. *Gondwana Research*, *24*(3–4), 1276–1282. https://doi.org/10.1016/j.gr.2013.02.008

Yang, X. N., Liu, J. R., & Shi, G. J. (2004). Extinction process and patterns of middle Permian Fusulinaceans in southwest China. *Lethaia*, *37*(2), 139–147. https://doi.org/10.1080/00241160410005114

Yoshiya, K., Nishizawa, M., Sawaki, Y., Ueno, Y., Komiya, T., Yamada, K., et al. (2012). In situ iron isotope analyses of pyrite and organic carbon isotope ratios in the Fortescue Group: Metabolic variations of a Late Archean ecosystem. *Precambrian Research*, *212*, 169–193. https://doi.org/10.1016/j.precamres.2012.05.003

Zaw Win, Z. (1999). Fusuline biostratigraphy and paleontology of the Akasaka limestone, Gifu Prefecture, Japan. *Bulletin of the Kitakyushu Museum of Natural History*, *18*, 1–76. https://doi.org/10.34522/bkmnh.18.0_1

Zhang, B., Wignall, P. B., Yao, S., Hu, W. X., & Liu, B. (2021). Collapsed upwelling and intensified euxinia in response to climate warming during the Capitanian (Middle Permian) mass extinction. *Gondwana Research*, *89*, 31–46. https://doi.org/10.1016/j.gr.2020.09.003

Zhang, B., Yao, S., Hu, W. X., Ding, H., Liu, B., & Ren, Y. (2019a). Development of a high-productivity and anoxic-euxinic condition during the late Guadalupian in the Lower Yangtze region: Implications for the mid-Capitanian extinction event. *Palaeogeography, Palaeoclimatology, Palaeoecology*, *531*, 108630. https://doi.org/10.1016/j.palaeo.2018.01.021

Zhang, B., Yao, S., Wignall, P. B., Hu, W. X., Ding, H., Liu, B., & Ren, Y. (2018). Widespread coastal upwelling along the eastern paleo-Tethys margin (South China) during the middle Permian (Guadalupian): Implications for organic matter accumulation. *Marine and Petroleum Geology*, *97*, 113–126. https://doi.org/10.1016/j.marpetgeo.2018.06.025

Zhang, B., Yao, S., Wignall, P. B., Hu, W. X., Liu, B., & Ren, Y. (2019b). New timing and geochemical constraints on the Capitanian (Middle Permian) extinction and environmental changes in deep-water settings: Evidence from the Lower Yangtze region of South China. *Journal of the Geological Society*, *176*(3), 588–608. https://doi.org/10.1144/jgs2018-137

Zhang, G. J., Zhang, X. L., Li, D., Farquhar, J., Shen, S. Z., Chen, X. Y., & Shen, Y. (2015). Widespread shoaling of sulfidic waters linked to the end-Guadalupian (Permian) mass extinction. *Geology*, *43*, 1091–1094. https://doi.org/10.1130/G37284.1

Zhang, X. N., Sigman, D. M., Morel, F. M. M., & Kraepiel, A. M. L. (2014). Nitrogen isotope fractionation by alternative nitrogenases and past ocean anoxia. *Proceedings of the National Academy of Sciences*, *111*(13), 4782–4787. https://doi.org/10.1073/pnas.1402976111

Zhou, M. F., Malpas, J., Song, X. Y., Robinson, P. T., Sun, M., Kennedy, A. K., et al. (2002). A temporal link between the Emeishan large igneous province (SW China) and the end-Guadalupian mass extinction. *Earth and Planetary Science Letters*, *196*(3–4), 113–122. https://doi.org/10.1016/S0012-821X(01)00608-2

References From the Supporting Information

Bourbonnais, A., Lehmann, M. F., Waniek, J. J., & Schulz-Bull, D. E. (2009). Nitrate isotope anomalies reflect N_2 fixation in the Azores Front region (subtropical NE Atlantic). *Journal of Geophysical Research*, *114*(C3), C03003. https://doi.org/10.1029/2007JC004617

Bunn, S. E., Loneragan, N. R., & Kempster, M. A. (1995). Effects of acid washing on stable isotope ratios of C and N in penaeid shrimp and seagrass: Implications for food-web studies using multiple stable isotopes. *Limnology & Oceanography*, *40*(3), 622–625. https://doi.org/10.4319/lo.1995.40.3.0622

Carabel, S., Godinez-Dominguez, E., Verisimo, P., Fernandez, L., & Freire, J. (2006). An assessment of sample processing methods for stable isotope analyses of marine food webs. *Journal of Experimental Marine Biology and Ecology*, *336*(2), 254–261. https://doi.org/10.1016/j.jembe.2006.06.001

Chen, B., Joachimski, M. M., Sun, Y. D., Shen, S. Z., & Lai, X. L. (2011). Carbon and conodont apatite oxygen isotope records of Guadalupian-Lopingian boundary sections: Climatic or sea-level signal? *Palaeogeography, Palaeoclimatology, Palaeoecology*, *311*(3–4), 145–153. https://doi.org/10.1016/j.palaeo.2011.08.016

Craine, J. M., Brookshire, E. N. J., Cramer, M. D., Hasselquist, N. J., Koba, K., Marin-Spiotta, E., & Wang, L. (2015). Ecological interpretations of nitrogen isotope ratios of terrestrial plants and soils. *Plant and Soil*, *396*(1–2), 1–26. https://doi.org/10.1007/s11104-015-2542-1

Cremonese, L., Shields-Zhou, G., Struck, U., Ling, H. F., Och, L., Chen, X., et al. (2013). Marine biogeochemical cycling during the early Cambrian constrained by a nitrogen and organic carbon isotope study of the Xiaotan section, South China. *Precambrian Research*, *225*, 148–165. https://doi.org/10.1016/j.precamres.2011.12.004

Itihara, Y. (1992). Recent studies on ammonium in rocks. *The Journal of the Geological Society of Japan*, *98*(9), 885–899. (in Japanese with English abstract). https://doi.org/10.5575/geosoc.98.885

Kolasinski, J., Rogers, K., & Patrick Frouin, P. (2008). Effects of acidification on carbon and nitrogen stable isotopes of benthic macrofauna from a tropical coral reef. *Rapid Communications in Mass Spectrometry*, *22*(18), 2955–2960. https://doi.org/10.1002/rcm.3694

Lorrain, A., Savoye, N., Chauvaud, L., Paulet, Y. M., & Naulet, N. (2003). Decarbonation and preservation method for the analysis of organic C and N contents and stable isotope ratios of low-carbonated suspended particulate material. *Analytica Chimica Acta*, *491*(2), 125–133. https://doi.org/10.1016/S0003-2670(03)00815-8

Marconi, D., Weigand, M. A., Rafter, P. A., McIlvin, M. R., Forbes, M., Casciotti, K. L., & Sigman, D. M. (2015). Nitrate isotope distributions on the US GEOTRACES North Atlantic cross-basin section: Signals of polar nitrate sources and low latitude nitrogen cycling. *Marine Chemistry*, *177*, 143–156. https://doi.org/10.1016/j.marchem.2015.06.007

Nieder, R., Benbi, D. K., & Scherer, H. W. (2011). Fixation and defixation of ammonium in soils: A review. *Biology and Fertility of Soils*, *47*, 1–14. https://doi.org/10.1007/s00374-010-0506-4

Nishizawa, M., Tsuchiya, Y., Du, W., Sawaki, Y., Matsui, Y., Wang, Y., et al. (2019). Shift in limiting nutrients in the late Ediacaran–early Cambrian marine systems of South China. *Palaeogeography, Palaeoclimatology, Palaeoecology*, *530*, 281–299. https://doi.org/10.1016/j.palaeo.2019.05.036

Rafter, P. A., Sigman, D. M., Charles, C. D., Kaiser, J., & Haug, G. H. (2012). Subsurface tropical Pacific nitrogen isotopic composition of nitrate: Biogeochemical signals and their transport. *Global Biogeochemical Cycles*, *26*(1), GB1003. https://doi.org/10.1029/2010GB003979

Syvaranta, J., Vesala, S., Rask, M., Ruuhijarvi, J., & Jones, R. I. (2008). Evaluating the utility of stable isotope analyses of archived freshwater sample materials. *Hydrobiologia*, *600*(1), 121–130. https://doi.org/10.1007/s10750-007-9181-3

Tesdal, J.-E., Galbraith, E. D., & Kienast, M. (2013). Nitrogen isotopes in bulk marine sediment: Linking seafloor observations with subseafloor records. *Biogeosciences*, *10*(1), 101–118. https://doi.org/10.5194/bg-10-101-2013

Ventura, M., & Jeppesen, E. (2010). Evaluating the need for acid treatment prior to $\delta^{13}C$ and $\delta^{15}N$ analysis of freshwater fish scales: Effects of varying scale mineral content, lake productivity and CO_2 concentration. *Hydrobiologia*, *644*(1), 245–259. https://doi.org/10.1007/s10750-010-0121-2

Waniek, J. J. (2003). The role of physical forcing in initiation of spring blooms in the northeast Atlantic. *Journal of Marine Systems*, *39*(1–2), 57–82. https://doi.org/10.1016/S0924-7963(02)00248-8

Williams, L. B., Ferrell, R. E., Jr., Hutcheon, I., Bakel, A. J., Walsh, M. M., Krouse, H. R., & Krouse, H. R. (1995). Nitrogen isotope geochemistry of organic matter and minerals during diagenesis and hydrocarbon migration. *Geochimica et Cosmochimica Acta*, *59*(4), 765–779. https://doi.org/10.1016/0016-7037(95)00005-K

Yokoyama, H., Tamaki, A., Harada, K., Shimoda, K., Koyama, K., & Ishihi, Y. (2005). Variability of diet-tissue isotopic fractionation in estuarine macrobenthos. *Marine Ecology Progress Series*, *296*, 115–128. https://doi.org/10.3354/meps296115

Yokoyama, H., & Ishihi, Y. (2006). Variation in $\delta^{13}C$ and $\delta^{15}N$ among different tissues of three estuarine bivalves: Implications for dietary reconstructions. *Plankton and Benthos Research*, *1*(4), 178–182. https://doi.org/10.3800/pbr.1.178

Zaw Win, Z. (2000). Paleoenvironmental and paleogeographycal consideration on the Akasaka limestone, Gifu Prefecture, Japan. *Bulletin of the Kitakyushu Museum of Natural History*, *19*, 9–23.

Zhang, Y. Z., Huang, S. H., Wan, D. J., Huang, Y. X., Zhou, W. J., & Zou, Y. B. (2007). Fixed Ammonium content and maximum capacity of ammonium fixation in major types of tillage soils in Hunan Province, China. *Agricultural Sciences in China*, *6*(4), 466–474. https://doi.org/10.1016/S1671-2927(07)60071-6